RICE UNIVERSITY

Towards Photocurrent Production By Gold Nanoarrays with Self-Assembled Monolayer Coatings

by

Tzu-Yu Liu

A THESIS SUBMITTED
IN PARTIAL FULFILLMENT OF THE
REQUIREMENTS FOR THE DEGREE

Master of Science

APPROVED, THESIS COMMITTEE:

Matteo Pasquali, Professor
Chemical and Biomolecular Engineering
Chemistry

Howard K. Schmidt, Senior Research Fellow
Chemical and Biomolecular Engineering

Michael S. Wong, Professor
Chemical and Biomolecular Engineering
Chemistry

Douglas Natelson, Professor
Physics and Astronomy
Electrical and Computer Engineering

HOUSTON, TEXAS
JULY 2010

ABSTRACT

Towards Photocurrent Production By Gold Nanoarrays with Self-Assembled Monolayer Coatings

by

Tzu-Yu Liu

This thesis proposes to use optical rectennae (rectifying antennae) for generating electricity by harvesting solar energy. Rectennae have theoretical efficiency over 90 %, well above that of current photovoltaic devices. They could be built by arraying nano-antennae combined with a self-assembled monolayer for DC current rectification. Gold nanoarrays were built to absorb light by plasmonic resonance by depositing a gold layer on CdSe tetrapods or directly growing nanowires via template synthesis; various alkanethiolates were explored as rectifying units. The tunneling properties of alkanethiolates on gold nanoarrays were examined by electrochemical analysis. Preliminary photocurrent tests show that electric currents can be induced at different optical frequencies depending on the aspect ratios of the nanoarrays. However, gold contributes as an enhancement rather than an active material. Furthermore, by fitting the impedance spectroscopy data with equivalent electric circuits, the calculated tunneling barrier of the self-assembled monolayer on gold nanoarrays is ten times lower than on gold film, suggesting that the monolayer formed on gold nanoarrays is defective and cannot serve as a practical rectifying barrier. This concept will need further investigation to lead to an applicable photovoltaic cell.

Acknowledgement

First of all, I would like to thank my advisors Matteo Pasquali and Howard K. Schmidt. This thesis would not have been possible unless they guided me and supervised me out of dead-ends at times. I especially thank Matteo for always examining my research from a completely different and keen view, and Howard for spending so much time with me about research, life and the way to play the single-player sport: Science.

I thank my lab group members for significant discussions and building the greatest lab atmosphere: Nikta Fakhri, Budhadipta Dan, Natnael Behabtu, Anson Ma, Emanuela Tamburri, Marco Notarianni, Dmitri Tsentalovich, J Alex Lee, Jaewook Nam, Colin Young, Jim Wang, Francesca Mirri, and Amir Amini. I will always appreciate the times in C112, Space Science, Camden Vanderbilt, or just on Skype. Special thanks to Dr. Juan G. Duque for the best mentoring at my first beginning of the project, Alex Eukel and Damir Aidarkhanov for working and having fun together, Dr. Hitesh Bagaria for providing samples, and Dr. Wei-Shun Chang from Link's group for critical and professional comments.

I thank the staff in Chemical and Biomolecular Engineering for dealing with the paperwork and every administrative deadline. I especially thank Hazel Cole, who helps arrange the meetings and takes care of the whole group amazingly.

At last, I would like to show my gratitude to my dear family. I thank my parents for supporting me no matter which decision I have made, I thank my brother for being talented in bugging me while I was busy, or trying to escape from the army when I took vacation back home. And I thank my whole family and friends in Houston, Chicago and Taiwan for their love and support during these three years. Life became more interesting through those random talks and jokes with you guys in Camden Greenway #25307, RGA, Bissonnet Village, or on some random streets.

Table of Contents

List of Tables

List of Figures

CHAPTER 1

Introduction

As demand, cost, and competition for primary energy sources grow worldwide, managing energy deficiencies has become increasingly difficult. With the projected world energy consumption approaching a deficit of one terawatt (TW) [1], secondary energy sources are more important than ever before. Most secondary energy sources are renewable; they include solar power, wind power, hydroelectricity and biomass. Among these secondary resources, solar energy is the most abundant, capable of producing an estimated 120,000 TW of power hitting the Earth continuously [2]. Effective use of solar radiation has the potential to solve many current energy problems [3]. Unfortunately, low efficiencies and high costs have prevented the widespread use of solar power, limiting it to less than 0.1 % of present energy sources [2].

In order to capture sunlight and convert it into useable electricity, photovoltaic devices are used. When light from the sun strikes a photovoltaic device, photons are absorbed. If the photon energy is larger than the photovoltaic bandgap energy, the absorbed photon excites an electron-hole pair. These excited electrons are forced into an external circuit by a diode array, thereby generating electricity. To date, most photovoltaic cells are fabricated with silicon p-n junctions [4]. P-n junctions occur at the intersection of p-doped (hole-rich) silicon and n-doped (electron-rich) silicon. The p-n junction serves as a diode by forming an electron density barrier between the two types of silicon. These simple photovoltaic cells, known as single bandgap cells, are widely used in the industry.

Due to limited efficiencies and expensive fabrication, several concepts have been investigated for their potential to improve on the efficiency and reduce the costs associated with conventional solar cells in recent years. These techniques include multi-bandgap materials [5], polymers [6], thin film technologies [7], and optical rectification [8]. Optical rectenna (rectifying antenna) is unique from these concepts because it can theoretically exceed 90 % efficiency, which is more than any other concept [8]. Optical rectennae consist of two key elements: an antenna which absorbs incident light through collective resonance, and a diode that rectifies the alternating current (AC signal) to direct current (DC signal). Rectennae have achieved over 90 % efficiency at microwave frequencies [8], and the technology has the potential to achieve similar efficiencies in photovoltaic cells. However, fabricating optical rectennae with integrated rectifiers that can operate at optical frequencies (10^{15} Hz) has proven difficult. In order to resonate with an incident photon's wavelength, an optical rectenna must be no more than several hundreds of nanometers. In addition, the accompanying diode must be comparably small and fast enough to switch at optical frequencies. These difficulties associated with size have not yet been solved. To date, no practical optical rectennae have been reported [9].

When considering what materials to use for rectennae, the material's physical properties are important. Gold is an excellent candidate material for antennae arrays. Well-known for its plasmonic properties, gold resonates with incident light. This results in a strong photo-absorbance in the visible region [10]. Additionally, the ability to use gold sub-nanostructure arrays as antennae has already been demonstrated by Lin *et al.* [11]. To create a rectifying barrier, a self-assembled monolayer (SAM) is induced, forming a non-linear rectifying devices [12, 13]. SAMs on gold surfaces using thiolates (compounds containing sulfur) has been investigated for decades, and is a well understood phenomenon [14]; therefore, we used thiolates to form a SAM on our gold antennae array. It should be noted that an experimental gold-thiol photovoltaic cell that exhibits rectennae behavior has not yet been made.

In this thesis, a simple background of photovoltaic cells and a review of key supporting concepts (optical rectenna, plasmonic properties of gold, and self-assembled monolayers, and electrochemical characterization) is presented in Chapter 2. Fabrication of gold arrays photocell based on two methods and corresponding photocurrent tests are discussed in Chapter 3. The first method involves sputtering gold onto tetrapods (quantum dots which have tetrahedral structure); the second method involves electroplating gold nanowires through a nanoporous membrane. Chapter 4 studies the tunneling properties of different self-assembled monolayer coatings on gold nanostructures by electrochemical methods. A summary and suggested future work are prescribed in the last chapter.

Objective

The long-term goal of this project aims to develop a photovoltaic cell that converts light into current through optical rectification. Toward this, we fabricated gold nanoarrays as antennae, and applied a self-assembled monolayer (SAM) of thiolate compound as a rectifying barrier. We explored the feasibility of the rectennae concept by studying the morphology of the samples by AFM and SEM, measuring photocurrents under monochromatic lights, and determining the tunneling properties of the rectifying barrier.

CHAPTER 2

Literature Review

2.1 Evolution of Photovoltaic Cells

Since Becquerel discovered the photovoltaic effect in 1839, people have sought to use the sun as enormous energy source. With an estimated flux of $1.2x10^5$ TW, solar power represents the most abundant renewable energy: three orders of magnitude higher than primary energy uses [15]. However, solar radiation is dispersed across a broad spectrum of wavelengths, and to capture solar energy efficiently, devices must be made with specific wavelengths in mind. The solar spectrum covers the wavelength from 250 nm to 2500 nm, but most irradiance occurs in the visible region (450 nm to 800 nm). Figure 2.1 shows the solar spectrum at airmass equal to 1.5 (AM 1.5) and its average power distribution [2]. Airmass is defined as the optical path length of light passing through Earth's atmosphere from a celestial source. It is relative to airmass at the zenith at sea level, which is defined as 1 (AM1). The region above Earth's atmosphere is AM0, and at horizon is about AM38.

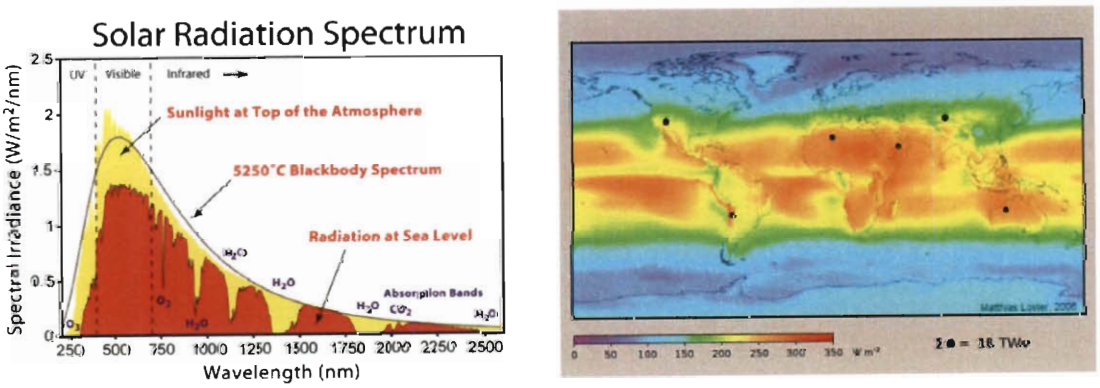

Fig. 2.1 (a) Solar AM 1.5 Spectra. (b) Average solar irradiance on Earth (unit: W/m^2) [2].

Photovoltaic cells are classified into three generations according to their efficiency and cost. First generation photovoltaic cells are primarily fabricated with crystalline silicon, using single bandgap technology. These photovoltaic cells have moderate efficiencies, but are prohibitively expensive. Second generation photovoltaic cells use thin film technologies to greatly reduce cost, but cannot match the moderate efficiencies of the first generation photovoltaic cells. Third generation photovoltaic cells are now achieving record efficiencies at relatively low costs by either blending the techniques used in the first two generations photovoltaic cells, or through novel, non-conventional techniques.

2.1.1 First Generation – Crystalline Silicon Cells

Since Pearson *et al.* created the first silicon solar cell in 1954, silicon has been the primary material used in photovoltaic cells [16]. These solar cells use bandgap absorption to exploit silicon's 1.1 eV bandgap. An electron-hole pair (exciton) can be produced by incident light whose energy is larger than the bandgap of silicon. To prevent the newly excited electron in the conduction band from recombining with the newly created hole in the valance band, an electric field is introduced in the depletion region of a p-n junction (diode) (Fig. 2.2 (a)). By doping silicon with different impurities, (potassium or other group V elements for n-type, and boron or other group III elements for p-type) the electron density of intrinsic (pure) silicon can be adjusted, creating positive and negatively charged surfaces. When p-doped and a n-doped silicon layers are brought into contact, electrons diffuse from the n-layer to the p-layer, forming a depletion region (diode) that induces an internal electric field (Fig. 2.2 (b)). The photovoltaic effect occurs when a photon excites an electron in p-doped silicon to move from the valence band into the conduction band. The electrons prefer to flow through the depletion region towards the n-type region. Because of the depletion barrier, electrons cannot return to the p-type region without additional energy, forcing them towards an external load via the n-type. This process results in the conversion of light into energy.

Though widely used, there are many reasons that silicon is less than ideal for use in photovoltaic devices. Silicon is an indirect bandgap material. The wave vectors ($k = 2\pi/\lambda$, representing the wavelength and direction of wave propagation) of silicon's lowest conduction state and highest valence state are not the same. Figure 2.3 (a) shows the difference between an indirect bandgap and a direct bandgap material. In an indirect bandgap material, an electron that is excited out of the valence band does not travel directly vertically. Therefore, the electron needs a transverse momentum to get to the conduction band. This usually occurs due to absorption of an extra phonon, which takes time. However, direct bandgap materials do not require this step. Therefore, the highest absorption efficiencies are achieved with direct bandgap materials (CdTe, GaAs, etc). As shown in Fig 2.3 (b), the main loss processes occurring in a single p-n junction solar cell are thermalization loss (route 1), junction and contact voltage loss (2 and 3), and recombination loss (4) [17]. Thermalization loss occurs when an incident photon can only generate one electron-hole pair regardless of how much energy the photon carries. The excess energy is emitted as heat, resulting in poor quantum efficiency. To date, the highest efficiency ever obtained with silicon solar cells is 25 % [17]. Additionally, building solar panels with crystalline silicon is expensive. Converting silica (SiO_2) into silicon requires large amounts of energy, and the resulting silicon wafers are brittle and thermally mismatched to their glass coversheets [18]. The qualities of silicon make the costs associated with manufacturing first generation PV cells considerable.

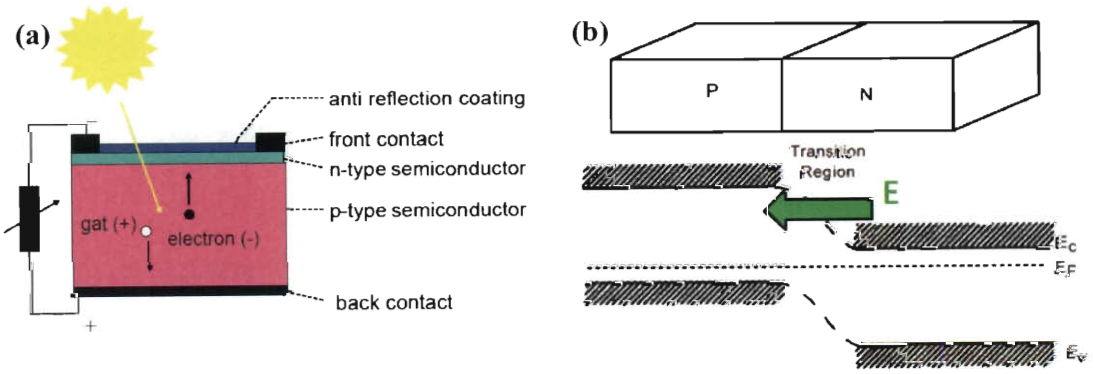

Fig. 2.2 (a) Basic geometry of solar cell and (b) depletion region formed at the p-n junction works as a rectifier (diode). Reproduced from Ref. [2, 4].

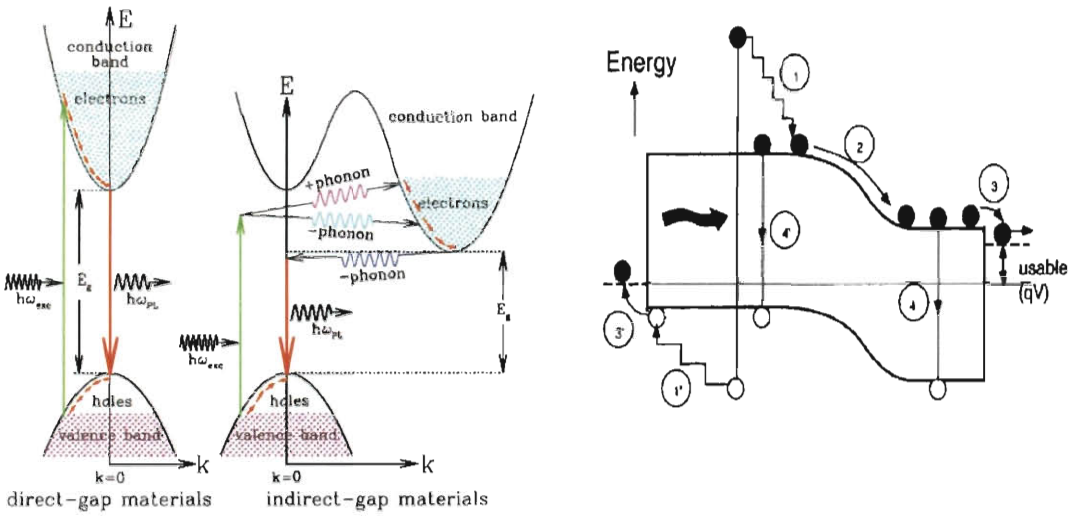

Fig. 2.3 (a) Energy diagram for direct and indirect bandgap materials. (b) Loss processes in a standard p-n junction solar cell. Reproduced from Ref. [17, 19].

2.1.2 Second generation – Thin Film Cells

By developing materials that can be fabricated at room temperature, second generation solar cells eliminate the costly high-temperature procedures used in the production of first generation solar cells. In most second generation photovoltaic devices, materials are coated as thin films (a few nanometer to micrometer in thickness) on silicon or glass substrates. III-V composite and amorphous silicon, as well as semiconductors like CdTe, and CIGS (copper-indium-gallium-selenide) are most used. Although thin-film processes can bring costs down to 0.5 USD/W, solar efficiencies are often rather low (less than 10 %). To achieve a high efficiency, low cost option, a third generation of solar cells has been created (Fig. 2.4).

2.1.3 Third Generation – Non-conventional and Advanced Thin-film Cells

Multi-junction and direct bandgap materials, such as GaAs and other II-VI materials, are some of the latest third generation photovoltaic devices [17]. Multi-junction photovoltaic devices feature multiple different bandgaps, allowing photon absorption across a wide range of wavelengths. These devices capture residual energy left after the initial photon absorption by adding additional bandgap(s). This allows a single photon to excite more than one electron, a significant improvement over first generation photovoltaic devices that excite only one electron per photon (due to a single bandgap). Multi-junction third generation PV devices are often made using composites of two or more materials.

Several new concepts also appear in third generation photovoltaic devices: (1) non-conventional PV cells based on quantum and nanostructure concepts, up/down converters, thermophotonics, hot-carrier cells, etc [17]; (2) organic materials like polymers used on electrode modification or dye-sensitized solar cells (DSSC); and (3) lattice-mismatched materials.

Figure 2.4 shows the efficiency and cost trajectory for each generation of photovoltaic devices [17]. First generation photovoltaic devices are characterized by high production costs (~350 USD/m^2) and moderate efficiencies (~20 %). Second generation PV devices are cheap to produce (~80 USD/m^2), but lack of efficiency (presently 5±10 %). Third generation photovoltaic devices are expected to combine the benefits of first and second generation photovoltaic devices, yielding cheap, highly efficient ones.

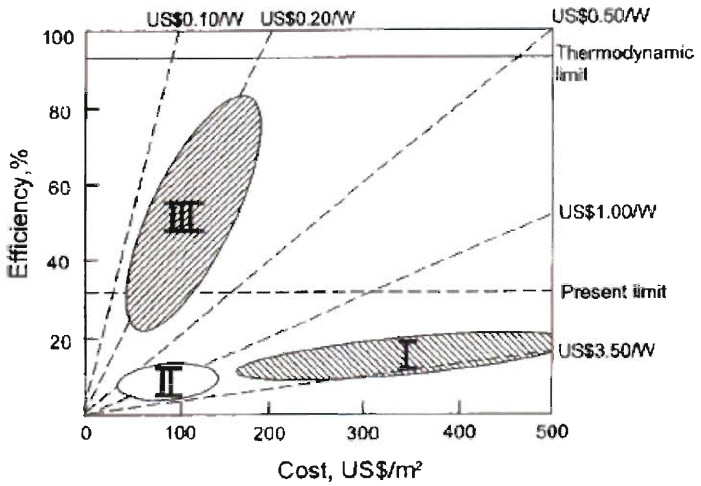

Fig. 2.4 Efficiency and cost projections for three generations of solar cells. Reproduced from Ref. [17].

Recent developments in nanotechnology have brought some of the most promising solutions for third generation photovoltaic devices closer to reality. Optical rectennae (rectifying antennae operating in the optical regime) have long been considered an ideal solution for solar energy harvesting. In concept, a rectenna captures light as a resonant antenna. The energy absorbed is then extracted by a rectifying barrier, creating a DC signal. Rectennae have no junction excitation limits, allowing for theoretical efficiencies over 90 % [20]. Further details are presented in the next section.

2.2 Optical Rectennae

2.2.1 Rectenna Concept

In 1972, Bailey proposed a radical new method of collecting energy that focused on capturing electromagnetic energy as a wave [21]. Bailey's new device featured an antennae array accompanied by a rectifying barrier. Because the device relies on electromagnetic oscillation, its efficiency is not inherently limited by bandgaps (unlike most modern PV devices). The device, termed a 'rectenna', was later built by Brown [8].

As shown in Fig 2.5, Bailey's rectenna uses an array of tapered absorber elements for antennae. Each antenna is attached to a half-wave rectifier (diode). Electromagnetic waves will resonate with the rectenna's $\lambda/2$ or $\lambda/4$ dipole antennae, forming electrical standing waves. A rectifier, e.g. Schottky barrier at the metal-semiconductor (MS) contact, metal-oxide-metal (MOM), or other fast-switching diodes, is then used to rectify the antenna's AC signal into DC output.

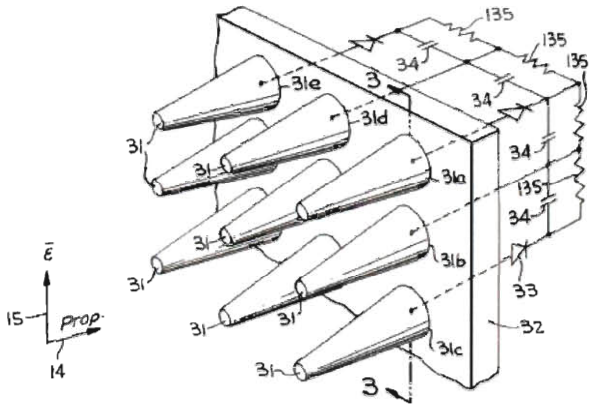

Fig. 2.5 Concept of rectennae. Conical dipole antennae, with each pair connected to a half-wave rectifier (can be formed by p-n junction), low pass filter, and load are shown [22].

The first functional rectennae (working in the microwave frequencies) was made by Brown in 1984 [8]. At a single wavelength frequency, Brown reported reception and conversion efficiencies close to 85 %. Since then, researchers have successfully managed to use rectennae to transmit power in microwave region [23-26]. Several authors have also claimed that 100 % collection efficiency in the transmission of power is possible [21, 24].

A simple block diagram of a rectenna is shown in Fig 2.6. Note that a non-linear rectifier, e.g. metal-insulator-metal (MIM) diode, would generate harmonics of the received frequencies and re-radiate from antenna back to space; therefore, a low pass filter is necessary to cut off higher frequencies.

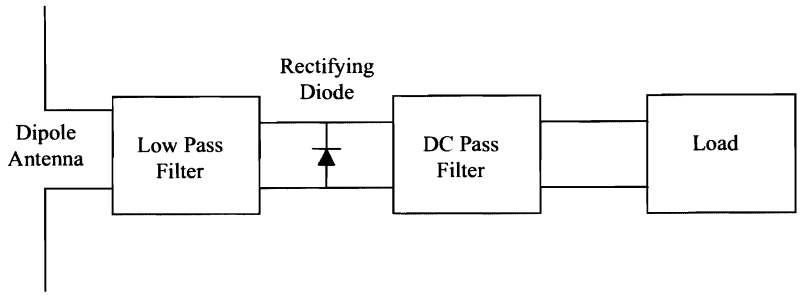

Fig. 2.6 Block diagram of rectenna application [24].

However, developing a rectennae device that works at optical frequency (~10^{15} Hz) is very hard. To date, the rectennae idea has not been demonstrated at visible frequencies yet. Several challenges have been discussed by Goswami and Corkish *et al.* [27, 28]:

1. *Antenna size*: To oscillate at the frequency of solar radiation, antennae need to have dimensions of the order of sub-micron range. The size issue brings up the difficulties of fabrication and quality control.
2. *Polarization*: The radiation of sunlight is incoherent and unpolarized, but a single linear antenna can only absorb a certain polarization of incident light. At least two orthogonal elements would be a first step to resolve polarization mismatch.
3. *Bandwidth*: The bandwidth of solar spectrum, which ranges from 0.2-2 μm (corresponding to approximate 150-1500 THz) is 60 %. However, the typical bandwidth of antennae is on the order of 15-20 % [29]. It will not only be difficult to capture the broadband spectrum; moreover, some harmonics of the long wavelengths which fall within the desired bandwidth of acceptance would need to be suppressed.
4. *Impedance matching*: In electric devices, each element needs to match its impedance with the connecting element(s). Impedance mismatch would cause the propagating wave to reflect back partially at the interface rather than transmit to the next element. It is particularly difficult for the rectifier, which is a non-linear component in the system, to match with the antenna. A low-pass filter might improve power flow continuity and matching, but the rectifier still needs to be ultra-thin (<10 nm). This is

the major challenge of the rectenna development right now, and details are discussed below.

In summary, the desired antenna materials must be chosen, so that they give broadband, circularly polarized absorption in the optical regime to catch most electromagnetic radiations. The rectifier materials will need to have very low impedance and fast switching to match with incident light and antenna.

2.2.2 Current Optical Rectennae Works

In 1996, the first experimental optical rectennae were demonstrated by Lin *et al.* [11]. N-doped silicon photocathodes were made into a parallel dipole antenna array on top of a p-doped silicon substrate through lithography (Fig 2.7). They successfully measured short-circuit currents at a single wavelength of incident light in the visible regime. By polarizing the incident light, it was shown that the cell has antenna behavior.

After this pioneering work, Berland *et al.* investigated coupling optical antennae with fast switching diodes [9]. They attained over 50 % efficiency by using a Schottky barrier as a rectifier on a micro-scale antenna array working in the microwave regime (10 GHz). It was further claimed that efficiency could be raised above 85 % by using a faster switching diode such as a metal-insulator-metal (MIM) rectifier. The project was ended by DARPA, and NREL re-started this work in late 2008. The schematic of their system is shown in Fig 2.8. Different shapes of optical antennae have been investigated, such as classic whisker diode tunnel junction [30-32], bow-tie antenna structures [33, 34], crescent [35], etc. While these shapes provide a more flexible range of absorbance, constructing the necessary rectifier becomes more difficult with increasing complexity.

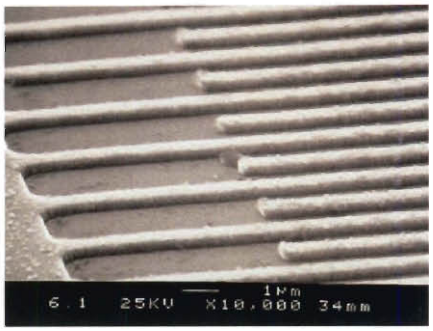

Fig. 2.7 Resonant nanostructure and rectification at visible wavelength [11].

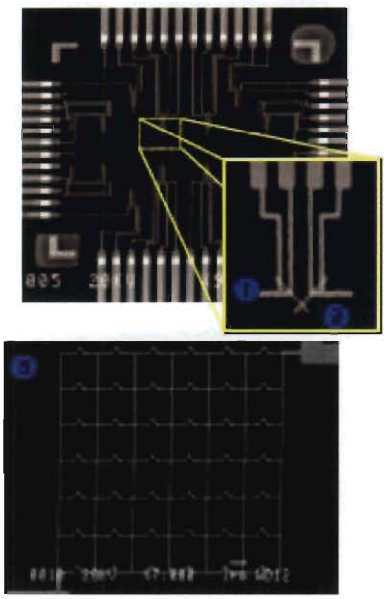

Fig. 2.8 ITN's optical rectenna scheme. (1) Antenna array to absorb complex waveform and scalable with frequency. (2) Non-linear planar MIM diode, which cutoff frequency is determined by the diode area. (3) Assembly of dual direction elements to capture complex polarization [9].

Due to their remarkable optical and electrical properties, carbon nanotubes are considered a potential target to capture light [36]. Ren's group at Boston University has demonstrated that a sparse array of multi-wall carbon nanotubes (MWNT) acts like optical rectennae and resonantly scatters visible light [37, 38]. Duque *et al.* have presented a novel optical rectenna device which combines a sparse array of CNT antennae, and rectifying barrier is formed by physisorbed surfactant molecules [39]. Figure 2.9 (a) show a schematic of three components of this device: (a) conductive CNT antennae, (b) rectifying barrier constructed by surfactant micelle, and (c) current collecting medium. The components are assembled as a liquid electrolyte Grätzel cell [40]. The results showed rectification of AC signal while under white light illumination,

indicating that the surfactant layer behaves as a rectifying barrier. A proposed energy potential diagram is described as in Fig 2.9 (b). Moreover, electrical current has been measured induced by light at visible region due to the successful charge separation.

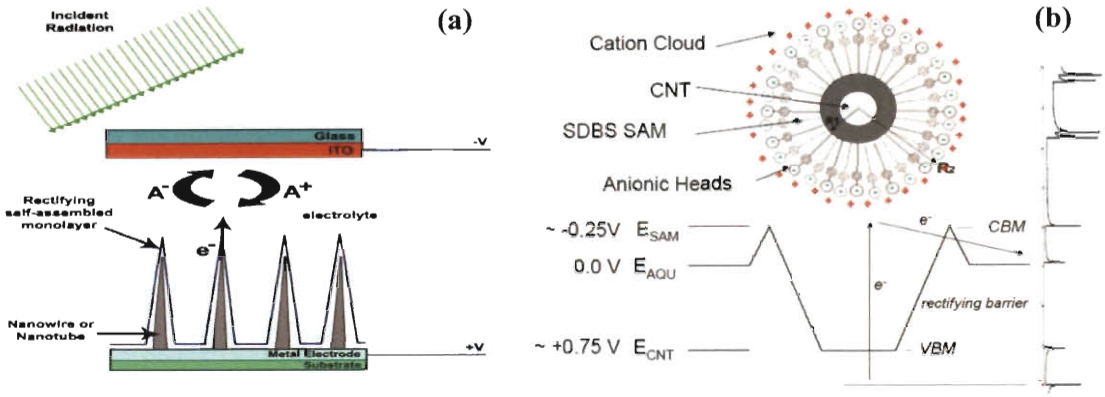

Fig. 2.9 (a) Electrochemical optical rectenna schematic, and (b) potential well created by a charged nanotube within an anionic surfactant micelle [39].

2.2.3 Our Rectenna System

Even though carbon nanotubes are easy to manufacture, it is hard to grow them in the proper configuration. In fact, only very small portion of MWNT act as antenna while others aggregate as bulk. Besides the control of orientation, the complex system of CNT has not been understood fundamentally. There are many kinds and types of CNT in a batch, which cause a broad light absorption. It is difficult to determine which kinds of tubes are being stimulated from the photocurrent data. Thus, we seek for other materials that are better understood from the fundamental viewpoint, easy to fabricate, have narrow size dispersity, and have narrow absorbance under visible wavelengths. Plasmonic materials have been well known for their ability to capture light [10]. The idea of surface plasmon resonance of plasmonic materials will be elaborated in the next section. Among those materials, silver and gold are widely used because their absorbance peaks fall in the visible region. However, silver has a tendency to oxidize and become inactive. On the other hand, gold is chemically stable, and relatively easy to obtain by electroplating (applying voltage to reduce metal ions into metals). Moreover, the self-assembled

monolayer (SAM) chemistry of thiolate compounds on gold surface is being widely used [12, 13, 41]. Hence, we first tried to fabricate a rectenna device with gold, in order to determine the potential of using plasmonic materials as high efficiency photovoltaic cells.

The Grätzel cell structure of our system can be divided into three components:

1. *Antenna*: Our gold antenna arrays are fabricated by two different methods. The simplest method to form gold nanorod antennae is to simply electroplate gold through porous membranes [42]. A more involved method to form gold antenna arrays is to sputter a thin layer of gold on the support of CdSe tetrapods [43]. CdSe tetrapods have a tetrahedral shape and are easily deposited on a flat surface. Their tetrahedral structure assures that when randomly dispersed on a flat surface, one arm will always be perpendicular to the surface, serving as a potential antenna.
2. *Rectifier*: Our rectifying barrier is constructed by a SAM of thiolate-gold interaction chemistry. The anionic tail group of the thiolate compound would form a higher potential barrier for electrons that acts as rectifier. Details of this will be addressed later.
3. *Electrolyte*: Different lengths of alkanethiolates and surfactants are tested to analyze the chemistry inside the cell. This will be discussed in the preliminary results.

Figure 2.10 (a) shows a cartoon schematic of a gold rectenna system using mercaptocarboxylic acid as the rectifier. An analogous electric circuit diagram (Fig. 2.10 (b)), indicating the corresponding electric components for the components in our optical rectennae system.

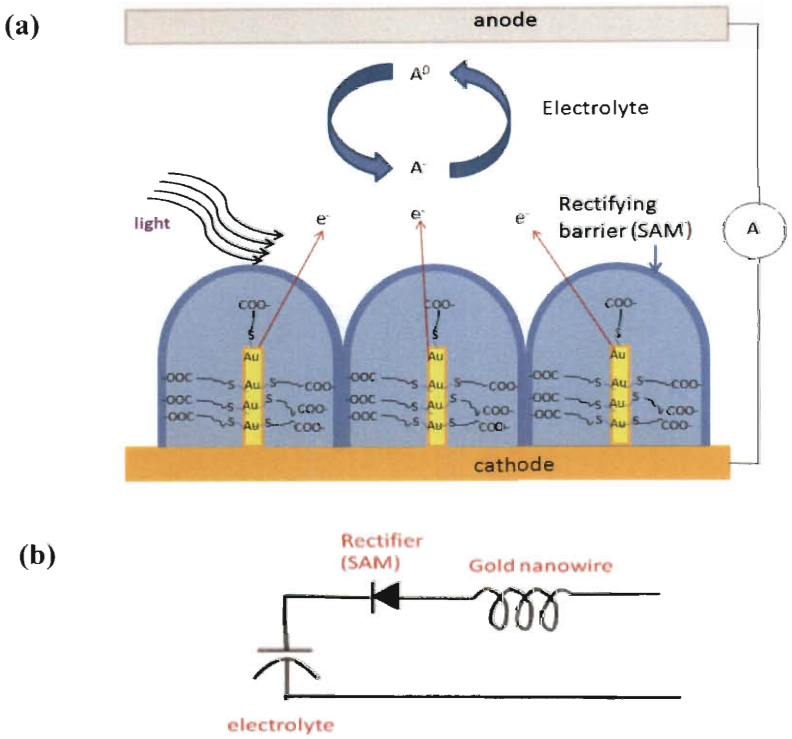

Fig. 2.10 (a) Schematic of Grätzel cell structure of gold rectennae system. (b) Equivalent electric circuit.

2.3 Surface Plasmon Resonance

The concept we are using for our rectennae is the surface plasmon resonance properties of gold. In this section, basic concept of SPR will be explained, and the SPR effect inside plasmonic nanoparticles and nanowires will also be discussed. At the last part, the electric field near the tip of a plasmonic nanowire will be illustrated, which is the driving force of separating electrons from the bulk when applying to a photovoltaic device.

2.3.1 Surface Plasmon Resonance (SPR)

Surface plasmon resonance (SPR) is a new phenomenon discovered in 20th century. The concept comes from the interaction of free conduction electrons in the metals with electromagnetic radiation. Plasmons are explained as an oscillation of free electron density in a metal. At characteristic resonance frequencies, meaning the wavelengths where the quantum energy carried by the photons exactly equals the quantum energy level of the plasmons, the electrons can sustain surface and volume charge density oscillations. Those electrons form surface plasmons (SP) and volume plasmons (VP), respectively. The resonance between incoming electromagnetic wave (such as light) and the metal itself can give rise to strongly enhanced optical near-fields that are confined near the metal surface. This property can be utilized for different kinds of applications [44]. In fact, far before people understood this phenomenon, as in 4th century A.D., the Lycurgus Cup already showed very interesting optical properties dictated by SPR [45]. The glassy mixture contains colloidal Ag-Au alloy crystals, and the size is so small (15-100 nm) that the Cup can scatter the light which results in dichroic effects (Fig. 2.11 (c)). When light shines from outside, the glass shows the reflected green light (Fig. 2.11 (a)). On the other hand, if light shines from inside, the gold absorbs the light corresponding to its SPR wavelength (~530 nm), and only transmits reddish color (Fig. 2.11 (b)).

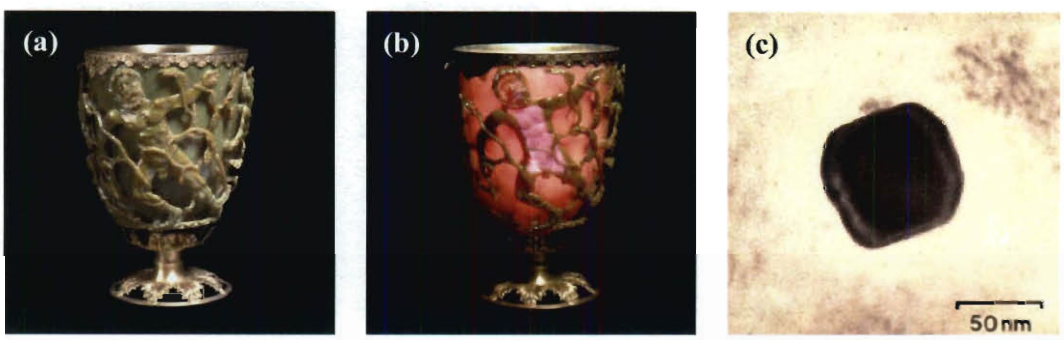

Fig. 2.11 Lycurgus Cup showed different color while shining from (a) outside and (b) inside. (c) TEM image of a Ag-Au alloy particle inside the glass [45].

The optical excitation of surface plasmon resonance was first formally observed in 1902, and the Maxwell's equations were mathematically solved by Mie in 1908 [46]. In 1968 Otto, followed by Kretschmann, successfully excited surface plasmon waves at the interface of planar metal film and dielectric materials, by using the method of attenuated total reflection by prism [47, 48]. The planar surface plasmon waves could propagate along the interface. The optical properties of metals can be described by a complex dielectric function that depends on the frequency of light. To get an idea of its basic physics, we start from Drude-Sommerfeld (D-S) theory, which predicts the real and imaginary dielectric constants of a metal as a function of wavelength. The D-S model gives quite accurate calculations in the infrared regime. However, in the visible range, higher-energy photons can promote electrons of lower-energy bands into the conduction band, and thus excite the oscillation of bounded electrons. Therefore, D-S model needs to be supplemented by the response of the interband transition. Fig 2.12 shows the real and imaginary parts of the dielectric constant of gold from theoretical calculations and experimental results by Johnson and Christy [44]. The negative real part indicates that light can penetrate through a metal only to a very small extent, and the imaginary part infers the dissipation energy due to the motion of electrons in the metal.

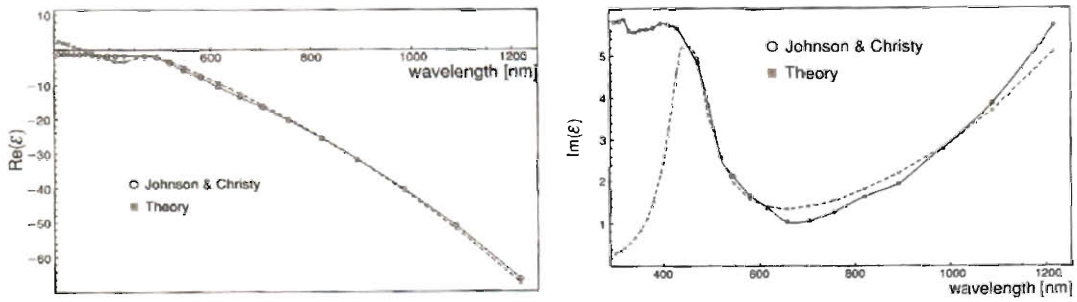

Fig. 2.12 Dielectric constants of gold as a function of wavelength [44]. Dashed lines represent the theoretical calculations. Solid lines are experimental data by Johnson & Christy.

By applying Fresnel formula with appropriate boundary conditions, the frequency-dependent surface plasmon wave vector k_{sp} is

$$k_{sp} = \frac{\omega}{c}\sqrt{\frac{\varepsilon_m(\omega)\varepsilon_s}{\varepsilon_m(\omega)+\varepsilon_s}}, \tag{3.2}$$

where ω is the wavelength, c is the speed of light, and ε_m and ε_s are the dielectric constants of metal and surroundings, respectively. Since ε_m is both negative and complex, and ε_s is usually positive, the momentum of surface plasmon k_{sp} is higher than that of a free space photon ($k_0 = \omega/c$). The SPs are generated on the metal surface by the mismatch between these two wave vectors, and couple to the light (Fig 2.13) [49]. Figure 2.14 shows the Otto and Kretschmann configurations used to induce SPs experimentally. A prism is placed either by the metal side or dielectric material side. As shown Fig 2.13 (b), when the incident angle goes beyond the critical angle, which causes total reflection, the electromagnetic (EM) field in the z direction decays exponentially with distance, which is considered as an evanescent wave. The vibration of the electron gas within the metal layer will be excited and trapped in the x direction, and generates surface plasmons at the interface of metal and dielectric material surface. Strong coupling between light and surface charge would let the electrons propagate along the surface.

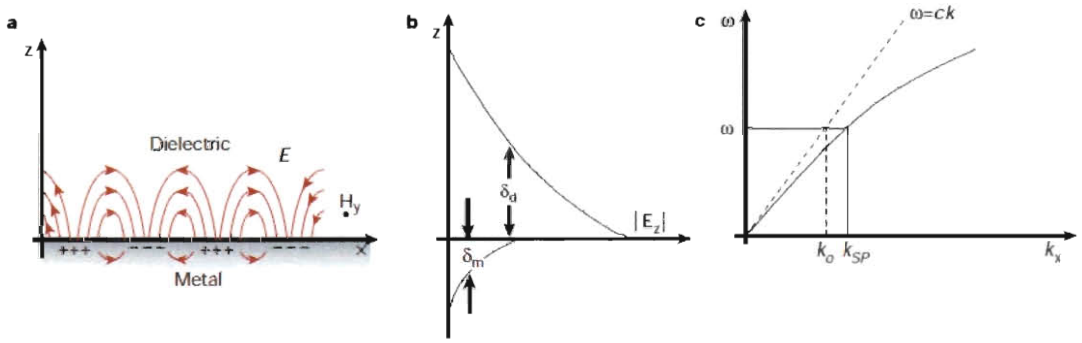

Fig. 2.13 SPs at the interface between a metal and a dielectric material. (a) Magnetic field (H) is on transverse direction, and the generation of surface charge requires an electric field normal to the surface. (b) The field in this perpendicular direction is said to be evanescent, indicating the bound, non-radiative nature of SPs, and prevents power from propagating away from the surface. In the dielectric medium above the metal, typically air or glass, the decay length of the field, δ_d, is on the order of half the wavelength of light involved, which is much longer than the decay length into the metal, δ_m. (c) The dispersion curve for a SP mode shows the momentum mismatch problem that must be overcome in order to couple light and SP modes together. Since the SP mode always lying beyond the light line, that is, it has greater momentum ($\hbar k_{SP}$) than a free space photon ($\hbar k_0$) of the same frequency ω [49].

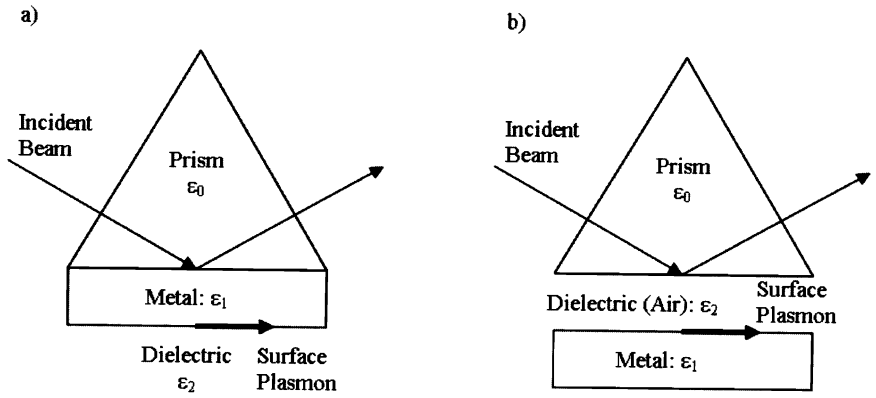

Fig. 2.14 Excitation of SP by (a) Kretschmann and (b) Otto configurations [44].

2.3.2 SPR in Nanoparticles and Nanowires

Recently, surface plasmon resonances in metallic nanoparticles, nanowires and other shapes (e.g., Crescent-Shaped [50] and nanostars [51]) are being explored for varied applications including sensors [52-54], waveguides [55-58], enhanced optical microscopy such as surface-enhanced Raman microscopy (SERS) [59, 60], subwavelength photonic devices, and even solar cells [61, 62]. A gold thin film on TiO_2 has increased the photocurrent response at incident wavelength from 500-600 nm [61]. A plasmonic layer coated on the surface of a conventional p-n junction photovoltaic cell can also enhance the absorbance of photons, and thus induce larger current [62].

When the wavelength of light is much larger than the particle size, it can induce standing resonance conditions as represented in Fig 2.15 [63]. The free electrons inside the particle are polarized from one end to the other end as the wave front passes by. This oscillation condition is determined from absorption and scattering. The electrons confined into nanoscale structures have specific oscillation modes due to geometry and electron density, so the surface plasmon resonance wavelength is very sensitive to the spherical diameter of nanoparticles, aspect ratio of nanowires, etc. Halas group at Rice University has successfully tuned the color of the Au nanoshells around SiO_2 cores by

controlling their core-shell ratios [64]. In addition, since SPR effect is associated with the local surroundings, the spectral position of the SPR of nanoparticles is observed to red-shift with increasing dielectric constant of the surrounding [65]. The local field enhancement and sensitive surrounding around those metal nanoparticles (usually silver and gold) allow the novel developments for biosensors, molecular sensing, and SERS.

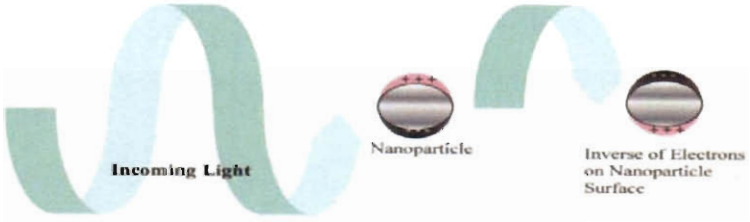

Fig. 2.15 Surface plasmons due to coherent interaction of the conduction electrons with light [63].

The SPR wavelength varies depending on its structure. Figure 2.16 (a) showed the absorbance spectra of gold nanoparticle colloids with different geometries. In anisotropic structures, like gold nanorods, the absorbance spectrum displays various resonance in response to the orientation of incident light [66]. In Fig 2.16 (b), the parallel polarized light (parallel to the long axis) shows resonance at longer wavelength, and perpendicular polarized light (perpendicular to the long axis) shows the absorbance at short wavelength. According to Eq. (3.3), the extinction coefficient is dependent on the depolarization factors based on the aspect ratio of the rod:

$$\gamma = \frac{2\pi N V \epsilon_m^{3/2}}{3\lambda} \sum_j \frac{(\frac{1}{P_j^2})\epsilon_2}{\left(\epsilon_1 + \frac{1-P_j}{P_j}\epsilon_m\right)^2 + \epsilon_2^2}, \tag{3.3}$$

where γ is the extinction coefficient, N the number of particles per unit volume, V the particle volume, ε_m the dielectric constant of the surrounding medium, λ the wavelength of the interacting light, ε_1 and ε_2 the real and complex parts of the material dielectric function, and P_j is the depolarization factors based on the aspect ratio of the rod [67].

Therefore, by changing the aspect ratio of the gold nanorods, one can easily tune the surface plasmon resonance, which is similar as for nanoparticles (Fig 2.17) [68].

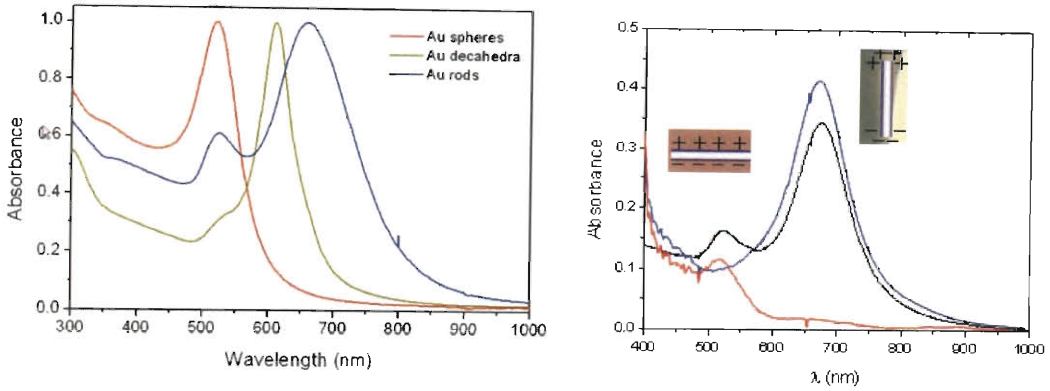

Fig. 2.16 (a) Absorbance spectrum of gold spheres, decahedrals and rods. (b) Plasmon resonance along and across the long axis of a nanorod [66].

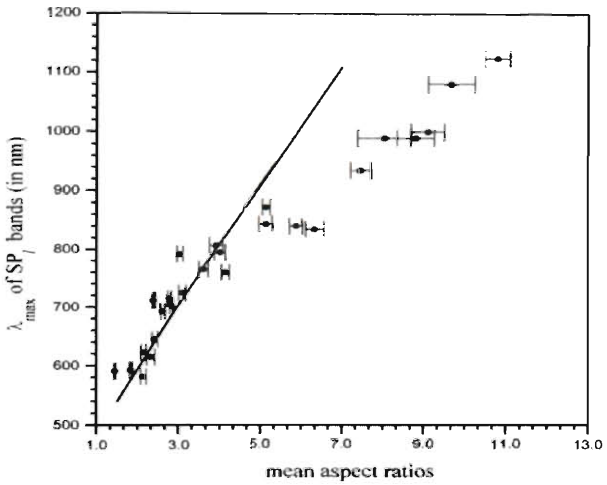

Fig. 2.17 Absorbed wavelength of longitudinal surface plasmon in nanorods as a function of mean aspect ratios. The transverse diameters of these prepared gold nanorods do not vary significantly from 10 nm [68].

One of the main applications of plasmonic nanowires is waveguides. Conventional fibers have problem transmitting light on the nanoscale because it reflects most information back rather than propagating through the fibers. Plasmonic materials,

however, can generate surface plasmons even at optical frequencies, and travel along nanoscale along nanowires, so they are very promising for waveguides. Stockman has done simulation about nanofocusing optical energy in tapered plasmonic silver waveguide [56]. He asserted that surface plasmon polaritons would propagate toward the tip of the waveguide, and asymptotically stop when they approach the tip but never reach it. Figure 2.18 shows a tapered silver cone in vacuum with excitation of 630 nm red light. A grating or a prism is used to excite the SPR at the end of the nanowire and propagate to the tip. From the Maxwell equations and appropriate boundary conditions at the interface, they found that both the phase velocity (v_p) and group velocity (v_g) tend to zero when approaching the tip. When the radius approaches zero at the tip, a singularity solution shows that the time to reach it is infinite. Figure 2.19 (a) shows a simulation result on the sharp tip with finite curvature tip (R'= dR/dz = -0.02 as shown in Fig 2.18). Consequently, the plasmonic modes accumulate energy at the tip and enhance the local optical field. The intensity of the local optical field is concentrated by more than 3 orders of magnitude at the surface of the metal tip (Fig. 2.19 (b,c)).

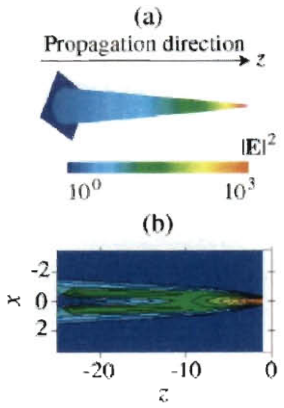

Fig. 2.18 (a) Geometry of the silver nanoplasmonic waveguide. Intensity I(r) of the local fields relative to the excitation field is shown by color bar. (b) Local electric field intensity in the longitudinal cross section of the system. The coordinates are indicated in the units of 100 nm, and the radius of the waveguide decreases gradually from 50 nm to 2 nm [56].

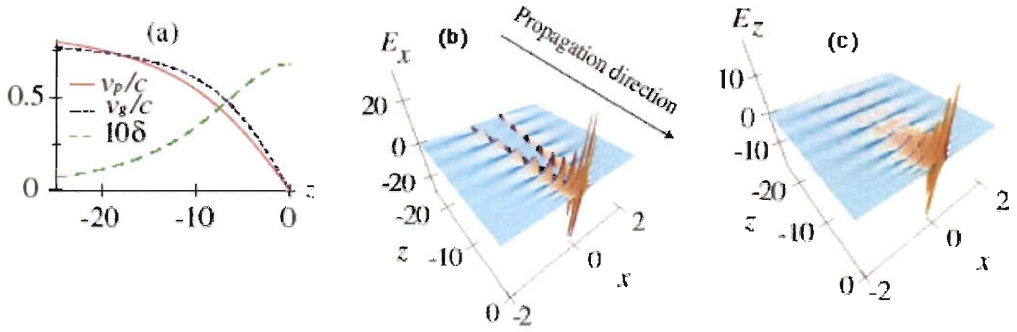

Fig. 2.19 Velocity and Electric field along the tapered nanowire. (a) Phase velocity v_p, group velocity v_g, and adiabatic parameter δ are shown as functions of the coordinate along the nanoplasmonic waveguide. Snapshot of instantaneous fields: normal component E_x (b) and longitudinal component E_z (c) of the local optical electric field. The fields are in the units of the excitation field [56].

The results let us think of an idea: What if we can collect those oscillating electrons at the tip? The highly enhanced electric field is likely to release some surface electrons into the bulk. The next problem is: How to prevent those electrons from reentering back into the gold? A rectifying barrier is thus required to separate the charges.

2.4 Rectifying Barrier (Charge Separation)

Once the electrons are excited and freely flow in the bulk, a rectifying barrier needs to be provided to prevent those electrons from reentering back into the gold. Otherwise, the efficiency would decrease significantly. It is similar as the charge separation of excited electrons and holes in photocatalysis. In the view of optical rectennae, the role of the rectifying barrier is also important to give sufficient separation. Since the self-assembly process of alkanethiolates on gold is well-known and easily manufactured, we use self-assembled monolayer as the rectifying barrier for the gold antennae.

2.4.1 Self-assembled Monolayer (SAM)

Self-assembled monolayer (SAM) by alkylthiolate chemisorption on gold surface has been well-known for decades [41]. Bare metal surfaces are prone to absorb extrinsic organic materials readily because those compounds lower the free energy between the metal and ambient environment. The absorbed layer can alter several physical and chemical properties, such as charge transfer [12, 13], wettability, electric barrier [69], or reactivity of the original surfaces [70]. The absorbates have head groups which prefer to assemble on the surface of the solid from liquid or gas phase, and begin to form crystalline or semicrystalline structure after hours [71]. The most extensively studied SAM are those made by absorption of alkylthiolates on gold, silver, copper, palladium, platinum and mercury [41]. The high affinity of thiols for those noble metal surfaces makes it possible to alternate the functionalities at the exposed interface. Figure 2.20 shows anatomy and characteristics of SAM of alkylthiolates on gold.

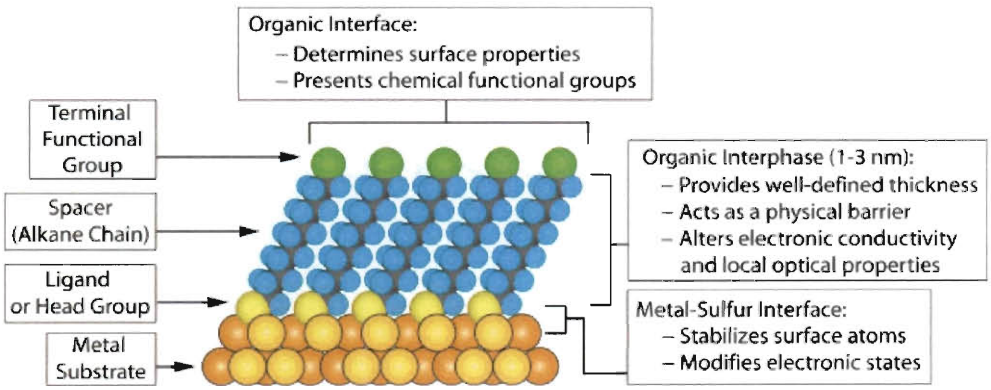

Fig. 2.20 Schematic diagram of a single-crystalline SAM of alkanethiolates supported on a (111) gold surface [41].

Compared to Metal-insulator-metal (MIM) diodes which are widely used in the microelectronics, SAM has more advantages to be manufactured at the nanoscale: (1) The thickness of SAM that is constructed by alkane CH_2 chain is usually only 1~2 nm; conversely, it is hard to fabricate ultra-thin MIM tunneling diode down to 10 nm. (2) Corresponding to the rectifier thickness, SAM has low dielectric constant, about 2, while

the κ value for MIM diodes is as high as about 20. Smaller dielectric constant would give higher permittivity of the electrons to tunnel through the dielectric layer and improve the impedance matching.

Since gold is inert to temperature or atmospheric O_2, and it also has very high affinity to bind with thiol groups, it is a very good candidate to serve as the antennae element [72]. In addition, it is simple to obtain thin film for spectroscopies and analytical techniques from gold, such as SERS, ellipsometry, QCM, etc. [41]. The protocol to form SAM is to immerse a freshly prepared substrate into a diluted (1~10 mM) ethanolic solution of thiols over 12 hours at room temperature. Several factors can affect the condition and the structure of the resulting SAM, e.g., solvents, temperature, concentration and purity of absorbate, immersion time, cleanliness and chain length. Some effects are still ambiguous. We assemble the SAM by using thiol compounds as electrolytes, and by immersing the gold substrate inside the electrolyte overnight. For experimental need, the thiols are, however, dissolved in the water instead of ethanol for photocurrent measurement, because of lower evaporation rate. Figure 2.21 shows the schematic diagram of the ideal absorption of SAM on gold nanowires with a rectifying barrier formed by anionic terminal groups.

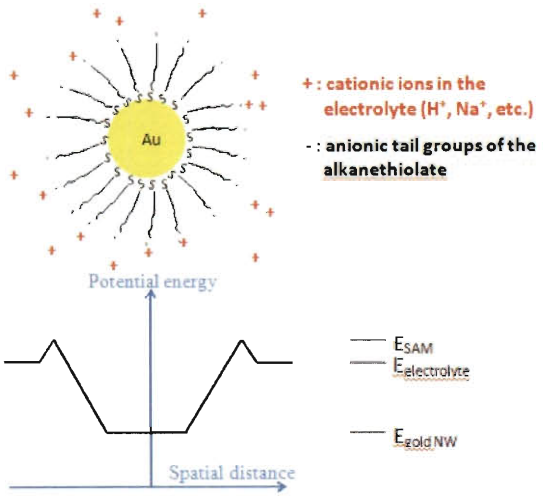

Fig. 2.21 Potential diagram of gold nanowires inside the thiol solution. SAM serves as a rectifying barrier.

2.4.2 Tunneling Properties of Self-Assembled Monolayers on Electrodes

One of the applications of SAM is to serve as a blocking monolayer on the metal electrodes. By inserting a structured hydrocarbon layer between the electrode and the electrolyte, such thin insulating monolayer films can be used for studying the charge-transfer mechanisms of simple electrode processes. The ions in the electrolyte can tunnel through the non-conductive hydrocarbon layer and cause faradaic reactions. The reduction current at any overpotential should decrease exponentially with the thickness of the monolayer as

$$i = i_0 e^{-\beta d}, \tag{3.4}$$

where i_0 is the current measured at the bare electrode, β is the electronic tunneling coefficient, and d is the thickness of the blocking monolayer film [73]. Typically, for alkyl chain length, each CH_2 will contribute a factor of 2 to 3 decrease in the rate constants [74]. For rectangular-shaped barrier, assuming β is independent from the driving potential, it can be expressed in related to the barrier height as

$$\beta = \frac{4\pi(2m)^{1/2}}{h} V^{1/2}, \tag{3.5}$$

where m is the free electron mass, h is Planck's constant, and V is the barrier height (eV). Plugging in the numbers, we can derive the relationship between β and V:

$$\beta = 1.025 V^{1/2}, \tag{3.6}$$

where β is in 1/Å and V is in eV. The value of the tunneling coefficient can be estimated by the electrochemical methods discussed in the next section.

2.4.3 Characterization of SAM by Electrochemical Analysis

Even though SAM are usually well-structured, pinhole and other defects may be created during the formation. These defects may impact the chemical and physical properties of the interface directly by making preferred paths for ion transport. A easy way to characterize the formation of SAM on electrode is by electrochemical analysis. Electrochemistry is concerned with the processes occurring at the interface between an electronic conductor (electrode) and an ionic conductor (electrolyte) [75]. The charges are carried from the reduction or oxidation of the electroactive redox species in the electrolyte under different applied voltages, i.e., $Ox + ne^- \leftrightarrow Red$. The ions, so-called faradic current, flow through the interface and show different behavior depending on the properties and modification of the electrode. Usually the electrochemical analysis is taken with a two-electrode system or three-electrode system. The two electrode system contains a working electrode and a counter electrode, while the three-electrode system has one more reference electrode to monitor the cell potential more accurately. Among the various electrochemical measurements, cyclic voltammetery (CV) and electrochemical impedance spectroscopy (EIS) are the mostly used methods for characterizing the SAM on the electrode.

Cyclic voltammetry (CV) is one of potential sweep methods. The potential (E) varies within a certain range, and the system records the faradic current (i) through the electrochemical cell. Every redox species has its own reduction potential. Therefore, a peak current would appear when the sweep reaches its characteristic potential. If the redox reaction is reversible, it will generate a pair of peak currents symmetrically on the cathodic (i_{pc}) and anodic side (i_{pa}). Cyclic voltammogram illustrates the types of electrochemical processes occurring and their corresponding species. Therefore, CV is a good indicator of the SAM formation. The CV curve changes from a reversible shape to an irreversible one in which the peak currents are substantially decreased. The rapid

electron transfer on the gold electrode is largely reduced by applying a monolayer to the gold surface. For example, in Fig. 2.22, a thin monolayer of 0.1 mM of octadecyl mercaptan deposited on 200 nm Au gives a huge blocking behavior compared with the bare gold electrode [76].

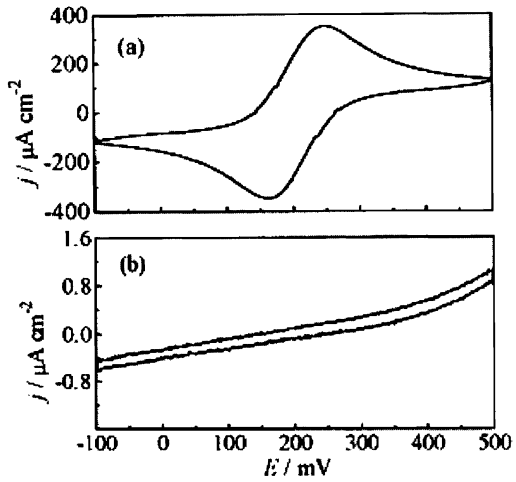

Fig. 2.22 Cyclic voltammograms of (a) bare Au and (b) a well-assembled monolayer of octadecyl mercaptan on gold. The electrolyte is 2 mM Fe(CN)63-/4- in 0.1 M KCl. Scan at 100 mV/s [76].

The CV method drives the electrode to a condition far from equilibrium, and it may destroy the interface if it is not well-formed. Contrarily, electrochemical impedance spectroscopy (EIS) exploits small perturbation on the system. EIS perturbs the cell with a small alternating signal from equilibrium, and observes how the system responds to this perturbation and returns to steady state [75]. This technique can measure over a wide range of time scales (usually measured by frequency). Since it is always operated near to equilibrium, it simplifies the kinetics and diffusion within the system without applying too much overpotential. AC voltammetry is a variation of EIS. A conventional three-electrode system is used in these experiments. The potential program imposed on the working electrode is a dc mean value E_{dc} (usually set at open circuit potential), with a small sinusoidal component of alternating signal, E_{ac}. The magnitude of the AC component of the current at different frequency of E_{ac} and its phase angle with respect to E_{ac} are measured.

\

The results can be plotted in either Bode plot or Nyquist plot. Bode plot displays the log value of absolute impedance and phase angle against log value of frequency ($\log | Z |$ and ϕ vs $\log \omega$), while Nyquist plot shows the imaginary impedance against real impedance at different frequencies (Z_{Im} vs. Z_{Re}). To analyze the EIS data, one represents its performance by an equivalent circuit composed of resistors, capacitors and other elements. This circuit demonstrates the same amplitude and phase angle as how electrochemical cell responds to the perturbation. Different applications, i.e., coating, corrosion, batteries, etc., have their representative equivalent circuit setups. As shown in Fig. 2.23 (a), a frequently used cell to illustrate mixed kinetic and diffusion control is called Randles equivalent circuit. It contains a solution resistance (R_Ω) in series with a sum of double-layer capacitance (C_d) and a general faradaic impedance (Z_f). A usual way to represent Z_f is a series of a charger transfer resistance (R_{ct}) and a Warburg impedance (Z_w). R_{ct} indicates the interfacial electron transfer of the redox probe between the electrolyte and the electrode, and Z_w depicts the resistance to mass transfer within the electrolyte. If the mass transfer is not significant for the cell, the Randles cell can be simplified by eliminating the Warburg impedance (Fig 2.23 (b)). The Nyquist plot of a typical Randles cell is similar to Fig. 2.23 (a). The semicircle is correlated to the kinetic control of the system, i.e. the charge transfer, while the tail indicates the mass transfer control. The radius of the semicircle is the magnitude of the charge transfer resistance (R_{ct}), which is an important parameter to derive the tunneling coefficient. For the simplified Randles cell (Fig 2.23 (b)), the mass transfer process is not significant enough, resulting only a semicircle in the plot.

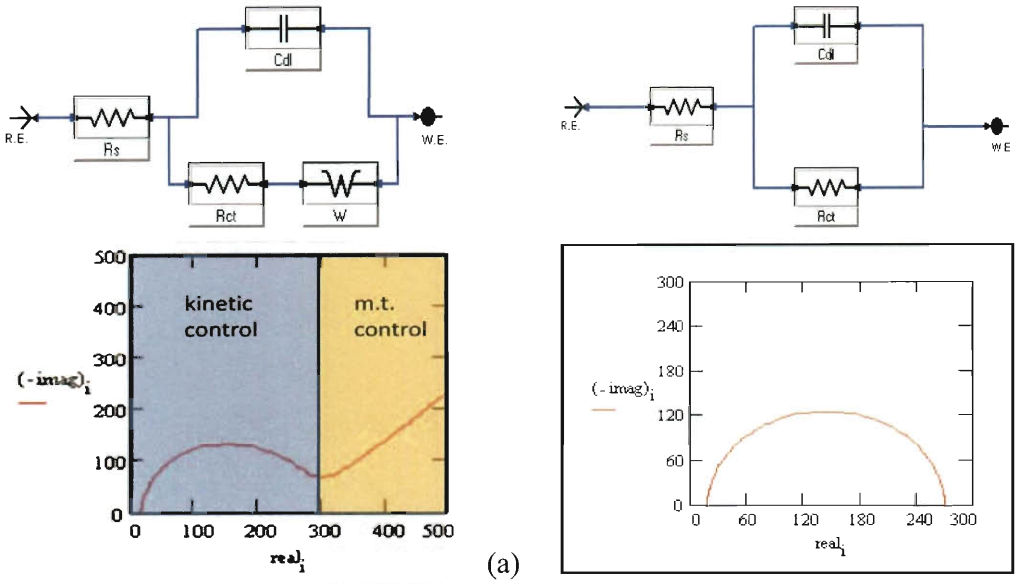

Fig. 2.23 Equivalent circuit and representative Nyquist plot for (a) Randles cell and (b) simplified Randles cell (adapted from Ref [77]).

To extract the tunneling barrier parameters from the equivalent circuit, the R_{ct} (Ω) can be expressed as

$$R_{ct} = \frac{RT}{A(nF)^2 k_{et} C}, \tag{3.7}$$

where R is the Boltzmann constant = 8.314 J/K-mol, T is the temperature in K, A is the electrode area in cm^2, n the number of transferred electrons per molecule of the redox probe, F the Faraday constant = 96586 C/mol, k_{et} the heterogeneous electron transfer rate constant of SAM modified electrode in cm/s, and C is the concentration of the redox couple in the bulk solution in mol/cm^3 [78]. And the tunneling coefficient can be obtained by inserting k_{et} into

$$k_{et} = k_0 e^{-\beta d}, \tag{3.8}$$

where k_0 is the electron transfer rate constant at bare gold electrode.

CHAPTER 3

Synthesis of Gold Structures and Preliminary Photocurrent Test

Two methods are used to yield gold arrays. One takes advantage of the tetrahedral structure of tetrapods by simply covering a layer of gold on them and the standing arms constructing a gold array. In the other method, gold ions are electroplated into nanopores of a membrane to form an embedded gold array, and the membrane is later dissolved to yield a free-standing gold array.

3.1 Experimental

3.1.1 Tetrapods

Nanoclusters and quantum dots show unique optical and electrical properties with reduced sizes [79]. After the techniques of making isotropic quantum dots, e.g., nanoparticles, became mature, state-of-the-art nanomaterial syntheses can grow anisotropic materials like rods, tetrapods, prisms, cubes, and other shapes [80]. The shapes of the nanostructures are based on the ratio of surfactants, injection volume, and time-dependent monomer concentration [81]. The structure of the tetrapod is topologically analogous to a sp^3 hybridized carbon atom, with four equivalent arms with an angle of 108.5° between each two arms. Anisotropic materials can be made by sequential growth of semiconductor dots and rods of different materials, with the potential for branched connectivity in each stage [82]. Many semiconductors show zincblende-wurtzite polytypism that can be utilized in fabricating heterostructures. The method to make tetrapods is to form a nucleus with cubic zincblende phase, and then subsequently grow in the hexagonal wurtzite phase.

Hot-injection is a widely applied method to generate quantum dots and nanoparticles. Tetrapods made of different materials have been investigated, such as CdTe, ZnO, CdS and CdSe. Among those nanocrystals, CdSe tetrapods are comparatively more difficult to fabricate than CdTe. Asokan *et al.* have successfully synthesized CdSe tetrapods with high shape selectivity and size uniformity [43]. They use cetyltrimethlyammonium bromide (CTAB), which has a head group of cationic NR_4 structure that can essentially control the shape of the quantum dots during the growth. The precursor of selenium, trioctlyphosphine selenide (TOPSe) combined with CTAB, is injected into an octandecene solution containing CdO and oleic acid at 300°C. Toluene is used as stabilizer. The growth proceeds at 280°C; the final material is recovered and washed with acetone. A mechanism of selective formation of CdSe tetrapods is also proposed (Fig 3.1).

We originally consider tetrapods as supports for gold because of their tetrahedral structure, that can let three arms standing on the surface still and one arm sticking out as antenna. The tetrapods are supplied by Dr. Hitesh Bagaria from Professor Michael Wong's lab. Since CdSe is also a semiconductor, it shows significant bandgap effect in the photocurrent responses, which will be discussed later.

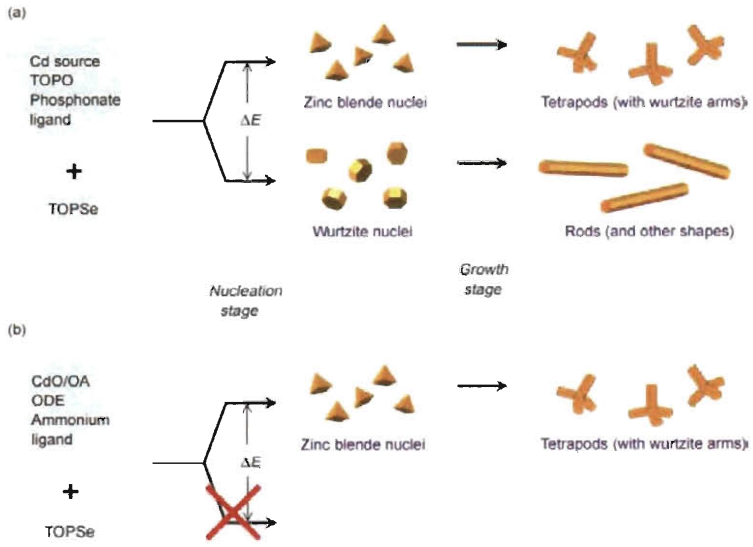

Fig. 3.1 Proposed mechanisms for the (a) nonselective and (b) selective formation of CdSe tetrapods with phosphonate or ammonium ligand [43]. The ones we are using is from the selective mechanism.

3.1.2 Template Synthesis

Preparation of nanomaterials by template-based method involves of the synthesis of materials inside the pores of a nanoporous membrane. The pores are usually cylindrical with uniform diameter. Depending on the chemistry of the sidewalls and the materials, nanowires or nanotubules can be obtained with desired length and diameter by controlling the growing process [42, 83, 84].

Two kinds of porous membranes are widely being used, ion track-etch polycarbonate (PC) membranes and anodic aluminum oxide (AAO) membranes. Polycarbonate membranes are fabricated by creating damage tracks in a polycarbonate sheet (e.g. by nuclear fission fragments), and then etching the tracks into pores [85]. By this means we can get randomly distributed pores with selectable density per unit area. On the other hand, AAO membranes are prepared via anodization of aluminium in an acidic solution [86]. Typically, commercial track-etch membranes have pore density about 10^9 pores per cm^2, and AAO membranes can be up to 10^{11} pores per cm^2 arranged in a quasi hexagonal close-packed array [87].

To grow nanowire or nanotube structures, template synthesis is a common method besides atomic layer deposition (ALD) [88, 89]. Since template synthesis does not have many limitations or requirements, many materials can be synthesized by electro-deposition within the membranes, such as gold [68, 84, 90, 91], copper [92], nickel [93], Au/Sn composite [94, 95], etc. There are also several kinds of strategies that have been used with templates, including electrochemical deposition, electroless deposition, chemical polymerization, sol-gel deposition, and chemical vapor deposition [83]. Electrochemical deposition is usually used to grow nanowires, while electroless deposition is utilized with functionalized side walls to give nano-tubular structures. In our system, we first focus on synthesizing gold nanowires.

Two-electrode or three-electrode system can be applied for the electro-deposition step in template synthesis. The basic procedure is (1) coat a conducting film as a cathode on one side of the membrane, (2) immerse the precursor solutions to wet the pores from the other side, (3) apply voltage to initiate the electro-deposition within the pores, and (4) control the precursor material(s), voltage, current, deposition time and other factors to get the desired length and crystallinity. Gold nanowires can be fabricated as single crystalline or polycrystalline depending on the precursor gold solutions [96]. Figure 3.2 shows a typical trend of current with respect to deposition time that can be divided into three stages [97]. The current holds constant at stage I, since the ions are depositing inside the pores separately, and do not enhance the conductivity of whole solution. As the material growing out of the pores and forming "cap-like" hemisphere, the resistance becomes lower and the current increases dramatically (stage II). When those caps coalesce into a film, the current reaches a plateau and increases slowly with thicker film deposition (stage III). The typical thickness of polycarbonate membranes is about several micrometers, so in order to form about 500 nm-long wires for appropriate resonant antennae length, we need to keep the growth of nanowires in the stage I.

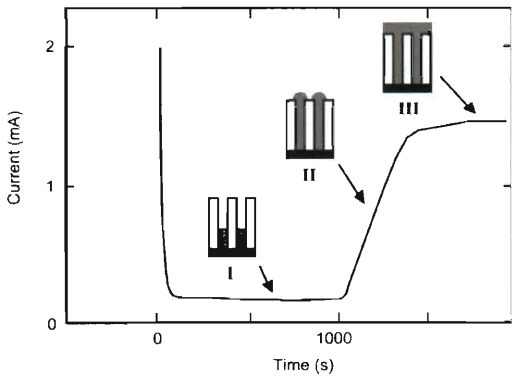

Fig. 3.2 Current versus time during electro-deposition of Ni nanowires [97]. Three stages are shown due to the different conditions of the growing materials.

3.1.3 Photocathode Preparations

Figure 3.3 shows three kinds of tetrapods varied in aspect ratios:

(a) Yellow tetrapods with mean average arm length of 12.5 nm and width of 2.5 nm. Its concentration is about 10^{16} particles/ml.

(b) Red tetrapods with mean average arm length of 40 nm and width of 2.5 nm. Its concentration is about 10^{16} particles/ml.

(c) Black tetrapods with mean average arm length of 12.5 nm and width of 5 nm. Its concentration is about 10^{15} particles/ml.

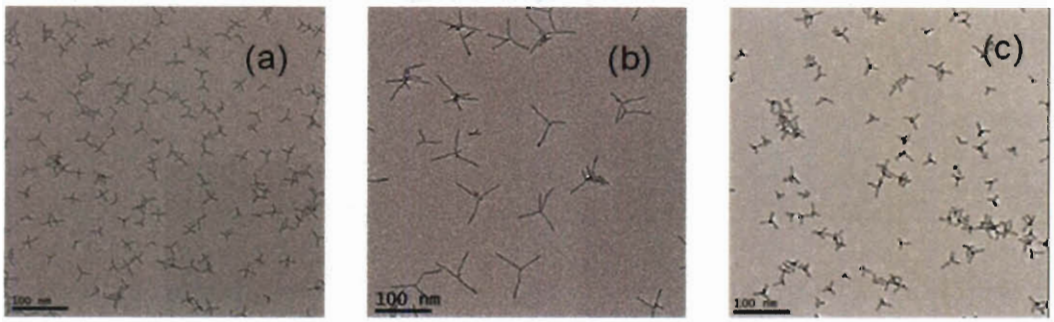

Fig. 3.3 TEM images of different shaped of CdSe. Color, length and width of the arms are (a) yellow, 12.5 nm, and 2.5 nm, (b) red, 40 nm, and 2.5 nm, and (c) black, 12.5 nm, and 5 nm, respectively.

To selectively deposit gold on tetrapods, Alivisatos group and Banin group make gold tips only on the end of the arms or single one arm [80, 98]. However, a thin smooth gold layer deposited on a rigid tetrapod array can also achieve it. The whole process is a bottom-up procedure. The substrates are indium tin oxide (ITO) for its transparency, and silicon wafer for its near-perfect smoothness. We spin-coated tetrapods on the substrates, and the vertical tetrapod arms would act as antennae. To test the possibility of surface plasmon resonance of gold thin film, a bottom gold layer was sputtered on the substrate (10 nm Au on ITO, or 7.5 nm Pt and 75 nm Au on silicon for better adhesion) by sputtering machine (CrC-150 Torr International, Inc.). 10 μL of each kind of tetrapods was then spin-coated on it, and washed by 2-propanol twice under spinning. To verify the

hypothesis, another 5 nm or 10 nm of gold thin layer were selectively sputtered on the top, and ideally formed the gold antennae array, as shown in Fig. 3.4.

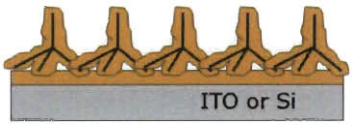

Fig. 3.4 Ideal gold array formed by sputtering gold on tetrapod supports.

Gold nanowires were fabricated by electroplating gold into ion track etch polycarbonate membrane (Sterlitech Co.). The pore diameter and nominal thickness are 30 nm and 6 μm, respectively. The pore density is about 6×10^8 pores/cm^2. Two kinds of gold electroplating solutions were used. One is commercial Orotemp 24 gold solution (Technic Inc.) which main compound is $KAu(CN)_2$, and the other is gold(III) chloride hydrate (99.999 % trace metals basis from Sigma Aldrich). Both were dissolved and diluted in water to desired concentrations. Copper electroplating solution is 1 M $CuSO_4$ (Sigma Aldrich) in water mixed with 2.5 v/v % of H_2SO_4.

Two-electrode system and constant electroplating voltage were used for all the electroplating processes. A constitution scheme of electroplating is shown in Fig 3.5. First, the membrane was attached to a poly-dimethylsiloxane (PDMS, from Sylgard® 184 silicone elastomer kit) piece to prevent it from folding. A 5/16" hole was punched in the middle of the PDMS to hold the electroplating solution. Second, a glass cylinder was filled with 1 ml of the electroplating solution, and clamped with PDMS and membrane. The electroplating cell was then hooked up with an external power supply. A magnetic stir was used to homogenize the solution.

As the block diagram described in Fig 3.6, a 100 nm gold film was evaporated on the rough side of the membrane. This conductive layer served as the cathode as well as the seeds for gold ions to deposit on. To enhance the mechanical support of the membrane, another copper film was electroplated directly on the gold thin film with a copper wire as anode. The thickness of the copper film is about 10 μm. A platinized

titanium rod (Anomet Inc.) and a gold wire were used as the counter anodes for $HAuCl_4$ and Orotemp 24 electro-depositions, respectively. Different lengths of gold nanowires were grown by controlling the deposition time and voltage. After the growth, the membrane was immediately dissolved in the methyl chloride for 20 min to harvest free standing gold nanowires arrays. For the convenience to characterize the samples, the dissolved samples are affixed on a SEM specimen holder by carbon tape.

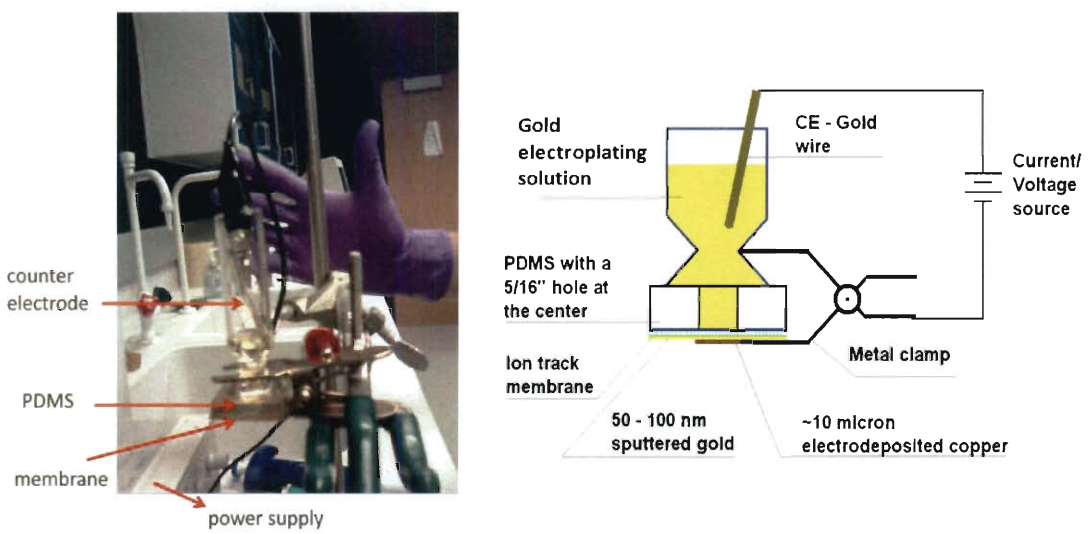

Fig. 3.5 Experimental setup and a schematic diagram of electroplating. A two electrode system was used. A holed PDMS is affixed between the membrane and a glass cylinder which was filled with electroplating solution. The cathode and the anode are further attached to a power supply.

.

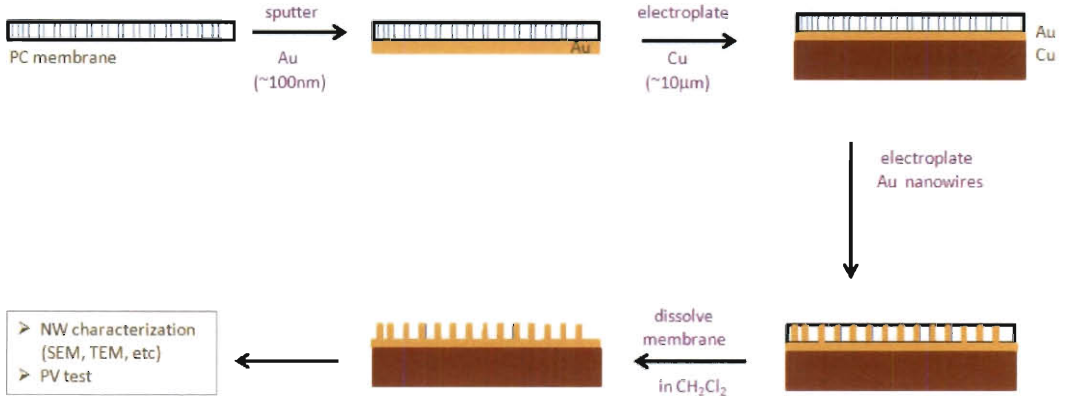

Fig. 3.6 Block diagram of growing free standing gold nanowires through polycarbonate membrane.

3.1.4 Photocurrent Measurement

After preparing the photocathode, we further glued a PDMS cylinder with a 1/8" hole at the center to hold the electrolyte fluid. We chose PDMS for its transparency to let illuminating light go through and shine on the cathode materials. Finally the counter electrode (usually ITO) was inserted into the electrolyte. The effective photocathode area is about 5 mm^2. Figure 3.7 (a) and (b) shows the top view of a real photovoltaic cell and a side-view cartoon to display the layers.

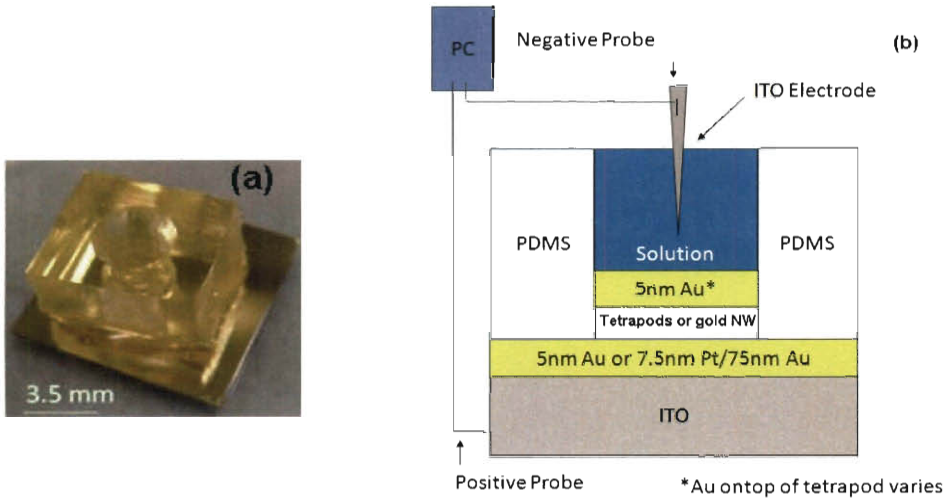

Fig. 3.7 Scheme of photocathode. (a) Photo of a photovoltaic cell. The substrate is a silicon chip sputtered with 7.5 nm Pt and 75 nm Au. (b) Side view of the photocell, showing each layer of the cell and the connecting circuit for measuring the short-circuit photocurrent.

The light source is broadband light generated by a 150 W xenon arc lamp with a ultraviolet-visible-near infrared monochromator (SpectroPro-150 from Princeton Instruments / Acton Research Corp. with wavelength from 100 nm to 1800 nm). A low-pass filter (455 nm, 695 nm, or 830 nm cut-off, all from Newport Corp.) is placed at the light output of the monochromator to filter out the second and higher orders of diffracted light. The current was measured by Keithley 485 picoammeter with a computer controlled Labview program. A polarizer was also placed at the output to test the polarization effect on the samples. A schematic diagram of photocurrent measurement

setup is shown in Fig 3.8. Because ITO is a transparent substrate, we measured the cell performance both in front and back configurations. The inserted orange box shows the back-lit configuration of the photocathode.

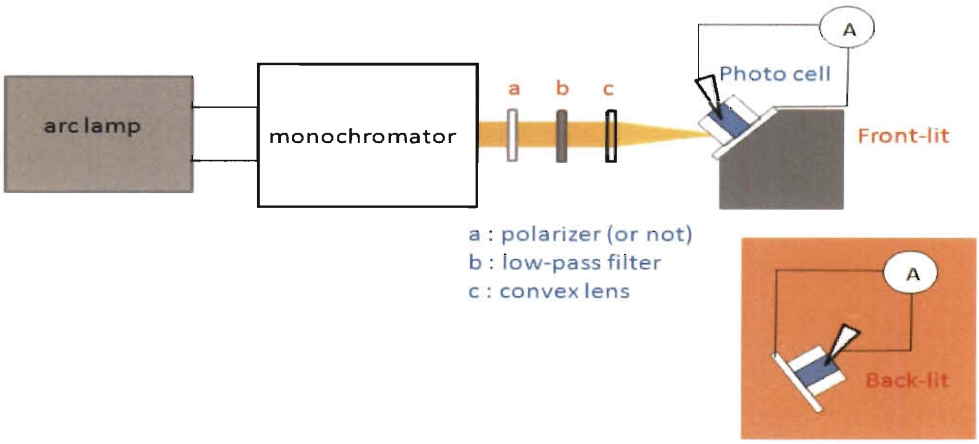

Fig. 3.8 Schematic diagram of the photocurrent measurement setup. A broadband white light is generated by xenon arc lamp, and goes through a monochromator to transmit narrow band of wavelengths. The output light is then going through a polarizer, low-pass filter, and focus by a convex lens before shining on the cell. A picoammeter is used to measure the current generated by the photovoltaic cell. The inserted orange box show the configuration of the back-lit setup.

3.1.5 Electrolyte

We tested many electrolytes. To prevent the electrolyte from evaporating too quickly during the illumination, we use water (instead of ethanol) as solvent; this makes it difficult to dissolve long chain alklythiolates. Therefore, we added 1 % of sodium dodecylbenzenesulfonate (SDBS) to improve the solubility. It is worth noting that the pKa value of thiol group and carboxylic acid group of 12-mercaptododecanoic acid are 6.1 and 10.6, respectively. The dissolved thiol solution is acidic (about 3~4), so we need to adjust the pH value to above 6.1 to let carboxyl group ionize and into a proton and COO^- group, where the latter form the anionic rectifying barrier. To meet this result, we added a small amount of NaOH to adjust the pH value to 7.

Therefore, several electrolytes we used are listed below:

- De-ionized water
- 1wt % (30 mM) SDBS in water
- Long chain alkylthiolate: 1 mM 12-mercaptododecanoic acid (DCC) in 1wt % SDBS in water, with NaOH to adjust pH value to neutral (pH = 6). Abbreviate it to S-T-NaOH.
- Short chain alkylthiolate: 1 mM 3-mercapto-1-propane (MPS).

TABLE 3.1 Structure and molecular weight of electrolyte compounds

Compound (concentration)	**Formula**	**Structure**	**Molecular weight (g/mol)**
SDBS (30 mM)	$C_{18}H_{29}NaO_3S$	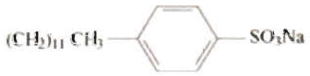	348.5
DCC (1 mM)	$C_{12}H_{24}O_2S$	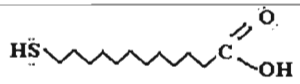	232.38
MPS (1 mM)	$C_3H_7O_3S_2Na$	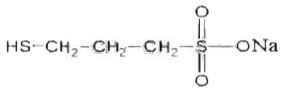	156.22

3.2 Gold Antennae on Tetrapods Supports

3.2.1 Morphology

Figure 3.9 (a) and (b) show AFM (atomic force microscopy, Nanoscope IIIa system, Veeco/Digital Instruments) images of spreading 10 μl red tetrapods on mica (Technic Inc.) in different concentrations, which is standard (used as received) and diluted by 20 folds, respectively. We can see that the standard solution forms like a thin film rather than individual tetrapods as we assumed, except for some rough regions which can be considered as broad random tips. In contrast, 20x diluted tetrapods show separated aggregates that have some arms protruding from the substrate. To ascertain that the

morphology does not change by varying the substrates, we also tried the same 20x diluted concentration on a silicon wafer sputtered with 7.5 nm Pt and 75 nm Au (Si/Pt/Au). Apparently, Fig. 3.9 (c) shows no difference from (b). Moreover, with bath sonication for 30 seconds, the aggregates broke into individual or smaller aggregates formed by 2-3 tetrapods (Fig. 3.9 (d)). The representative figures of yellow and black tetrapods of the same conditions are also shown (Fig. 3.9 (e) and (f)). All the samples were rinsed by 2-isopropanol after spin-coating to remove the excess surfactants within the solution. The thin films were served on the ITO substrate, and the spike arrays were tested on Si/Pt/Au surface.

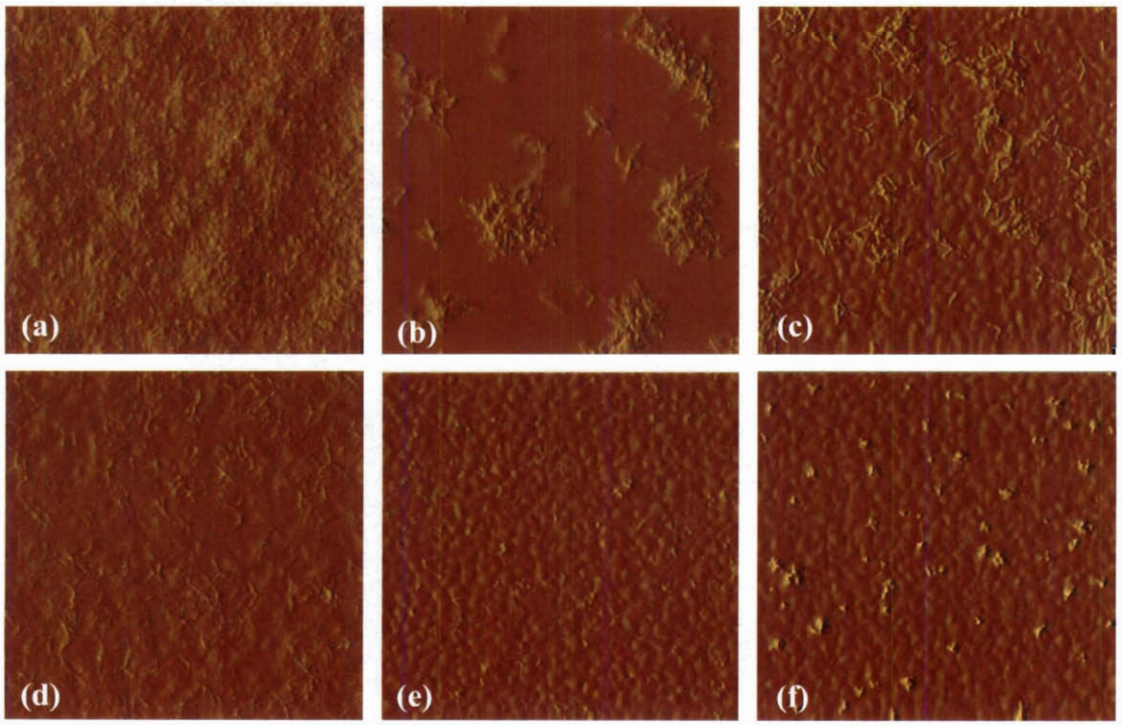

Fig. 3.9 AFM images of red tetrapods with (a) standard concentration on mica, (b) 20x diluted concentration on mica, (c) 20x diluted concentration on Si/Pt/Au. (d), (e) and (f) show the red, yellow, and black tetrapods of 20x diluted concentration followed by 30 s bath sonication on Si/Pt/Au, respectively. The dimension of all the images is 1 μm×1 μm.

3.2.2 CdSe Tetrapods on ITO Substrate

As the AFM images show, non-diluted CdSe tetrapods on the surface form a thin film with some rough regions. After sputtering 10 nm of gold, which serves as a thin film as well, the incident light can excite the free electrons on the surface of the gold thin film (~10 nm) to oscillate with the photons. And those electrons, with decent chance, can further get out of the gold bulk and serve as free charges inside the electrolyte. The SAM would rectify those electron flows and thus create dc current. However, since CdSe itself is a semiconductor that is usually used as an electron donor, and ITO is a degenerate n+ semiconductor (with high doping-level that makes it act like a metal), the electrons in both compounds can also easily be excited by the incident photons. Moreover, Schottky barrier can also possibly form at the interface of metal and semiconductor, namely, at Au-ITO or Au-CdSe interfaces. Combining those possible paths for the electrons, the photocurrent responses indicate multi-mechanisms due to the interactions between the materials (Fig. 3.11 and 3.12).

We have done photocurrent measurements by two kinds of sources. One is broad band white light, and another is monochromatic light by passing the white light through a monochromator. Figure 3.10 shows the white light response of black tetrapods sputtered with 5 nm of gold in SDBS electrolyte. Note the monochromator cut the intensity of white light even when it is not operating, leading to about an order of magnitude in current drop (from 10^2 nA to 10 nA). In this experiment, the white light was shone directly on the sample without going through the monochromator. We can see distinctive peaks appearing immediately after turning the light on and off, with each period for 30 seconds. We believe that the generated current is due to the multilayers forming from physisorption of surfactants on gold surface [99, 100], as well as the bandgap adsorption of CdSe and ITO. The anionic SDBS constructed a rectifying barrier to prevent electrons from returning back to the photocathode. Interestingly, despite being one order of magnitude more diluted in density, black tetrapods show ten times larger current than red or yellow tetrapods. Furthermore, the back-lit configuration (red trace) is more efficient

than the front-lit one (blue trace), and has a plateau at about 450 nA under continuous illumination. The difference between the directions of the incident light might due to the electrons of ITO substrate. With front-lit configuration, the photon energy is consumed layer by layer from the top to the bottom, which is gold, CdSe tetrapods, and ITO, respectively. This limits the photon energy that reaches ITO bulk and excites the electrons from it. In contrast, when shining from the bottom (back-lit configuration), ITO is the first layer to absorb energy, and thus more electrons are able to contribute for photocurrent. Same trend appeared in red and yellow tetrapods samples as well.

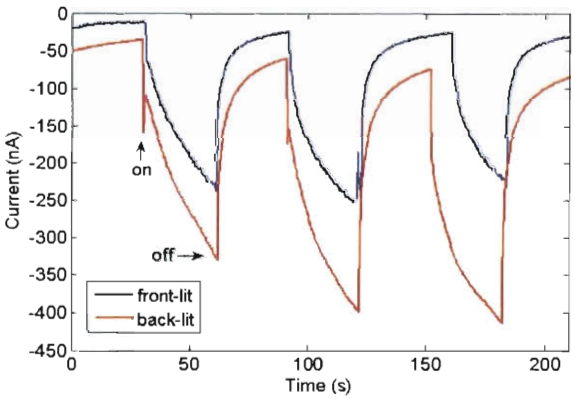

Fig. 3.10 White light response of black tetrapods sputtered with gold in SDBS electrolyte. The arrows indicate the time light was turned on and off.

To analyze the operating mechanism of the photocurrent response and confirm the hypothesis, we exposed the samples to the light as a function of wavelength by using a monochromator. The current responses are generally consistent with the absorbance spectrum of the tetrapods (Fig 3.11 (a)). This is due to the high density of CdSe tetrapods (10^{13} to 10^{14} particles on 5 mm^2 photocathode area) compared to that of the 10 nm gold. As shown in Fig. 3.11 (b), black tetrapods with sputtered gold have almost identical trace as absorbance figure. Contrarily, the control sample (without tetrapods, Fig. 3.11 (d)) had no current around the absorbance peak (625 nm), which confirms that tetrapods are the major resources of the photocurrent response. Interestingly, both control and tetrapods samples showed a strong peak mostly falling in 300~350 nm. The reason is not clear right now, but we speculate that it is due to the broad band gap (3.5 to 4.06 eV) of ITO, which

corresponds to 305 – 354 nm of light [101]. In addition, selective thiols can form SAM on ITO surface [102, 103], which can also be applied as a rectifying barrier of the ITO counter electrode inside the electrolyte which is partially illuminated.

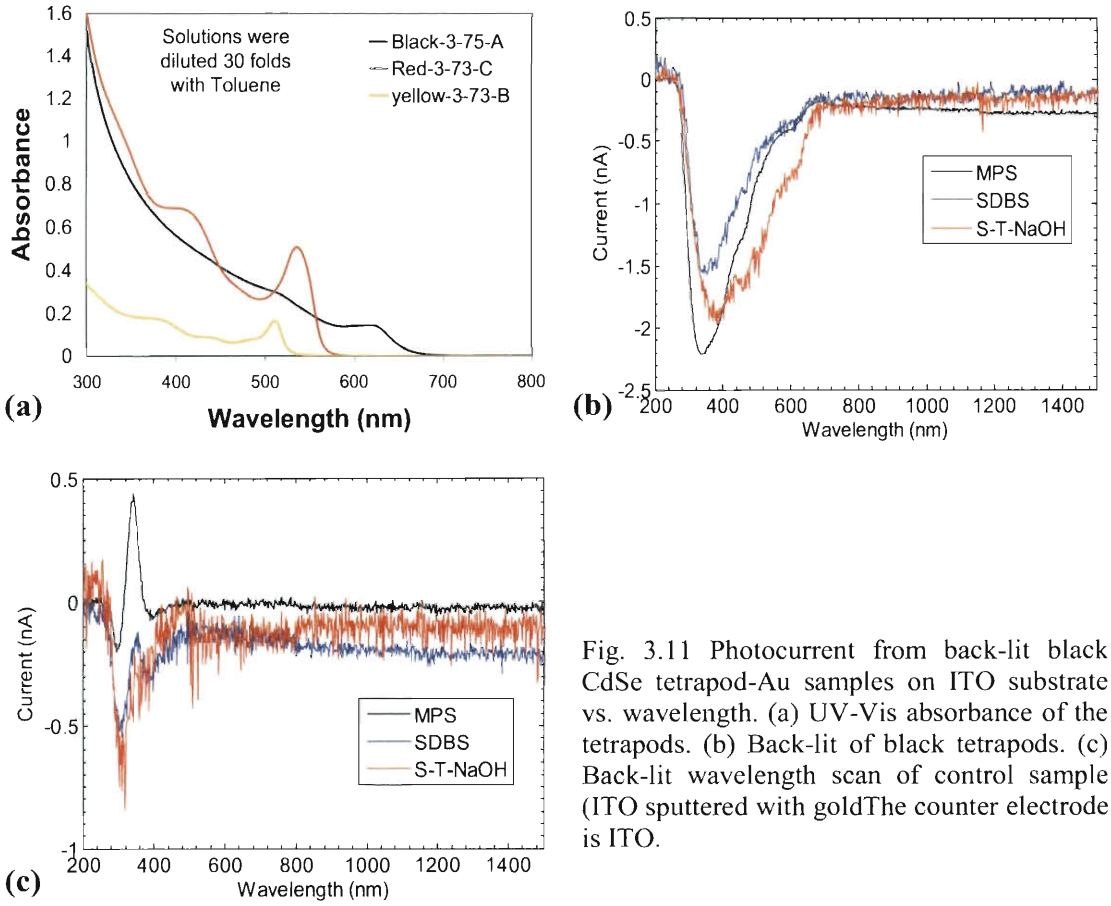

Fig. 3.11 Photocurrent from back-lit black CdSe tetrapod-Au samples on ITO substrate vs. wavelength. (a) UV-Vis absorbance of the tetrapods. (b) Back-lit of black tetrapods. (c) Back-lit wavelength scan of control sample (ITO sputtered with goldThe counter electrode is ITO.

We further discussed the multi mechanisms among the participating materials. Instead of the mostly contributing electrons from the CdSe semiconductor, the electrons of gold also participate in the current response. Gold is well-known for its absorption at visible region. Hence, several samples with the top layer of gold show higher photocurrent than that without the gold layer. However, some samples showed less current after adding the top gold layer. This phenomenon can be discussed from the directions of the generated current flows from gold and tetrapods, and different sizes of the tetrapods. With external batteries, we confirmed that positive current means that the

electrons are collected from the top counter electrode, while negative current indicates the opposite side. We observed that most peaks of the photocurrent responses are negative, inferring that the electrons from bandgap absorption of tetrapods (major current resource) prefer to be collected from the photocathode. Contrarily, there are two directions for the electrons of gold to flow. One is overcoming the SAM barrier and getting captured from the counter electrode (positive current); the other is to overcoming the Schottky barrier which possibly forms at the interface of the gold and the CdSe tetrapods, and being collected by the photocathode contact (negative current). Since the work function, electron affinity, and other properties of CdSe tetrapods with different shapes have not been investigated thoroughly, we are pressed to determine whether there is any Schottky diode formation at the interface among different tetrapods and gold, and thus determine the direction of the electron flow generated from the gold.

In black tetrapods case (shortest arm and length, Fig 3.11 (b)), consider its smallest dimension of structure, the black-CdSe thin film would be the thinnest among all kinds of the tetrapods. Therefore, the top sputtered Au (10 nm-thick) would nearly cover all the rough regions on the tetrapods surface and form a perfect thin film. Observed negative currents may indicate the formation of Schottky barrier at the interface of black tetrapods and gold. For CdSe crystal doped with In, the barrier height of the Au-CdSe Schottky diode is about 0.7 eV [104]; the typical thiol-gold SAM barrier is around 1 eV. It makes the free electrons of gold prefer to overcome the Schottky barrier and form negative currents. The SAM would act more like a hindrance barrier than tunneling barrier. It is consistent with that both samples in thiol solutions presented higher current than that in SDBS. This can refer to the better rectifying barrier by more compacted self-assembled monolayer forming between gold surface and thiol rather than surfactants [105].

Figure 3.12 (a) and (b) displays the data of yellow tetrapods without and with gold layer, respectively. Since the size of the yellow tetrapods is similar as black ones, negative currents were observed as well. Before sputtering gold layer, the major two negative peaks at 400 nm and 510 nm are identical with UV-Vis absorbance of yellow

tetrapods, except some blue-shifts due to the aggregation of the particles. However, after sputtering the gold, the SDBS figure remained the same, while currents above 510 nm were diminished for both thiol solutions. We infer that the electrons from gold prefer to overcome the SAM barrier. It might due to the lower SAM barrier compared to Schottky barrier of yellow tetrapods-gold contact. Those free electrons overcome the SAM barrier and produce positive currents that compensate the negative currents generated from the yellow tetrapods.

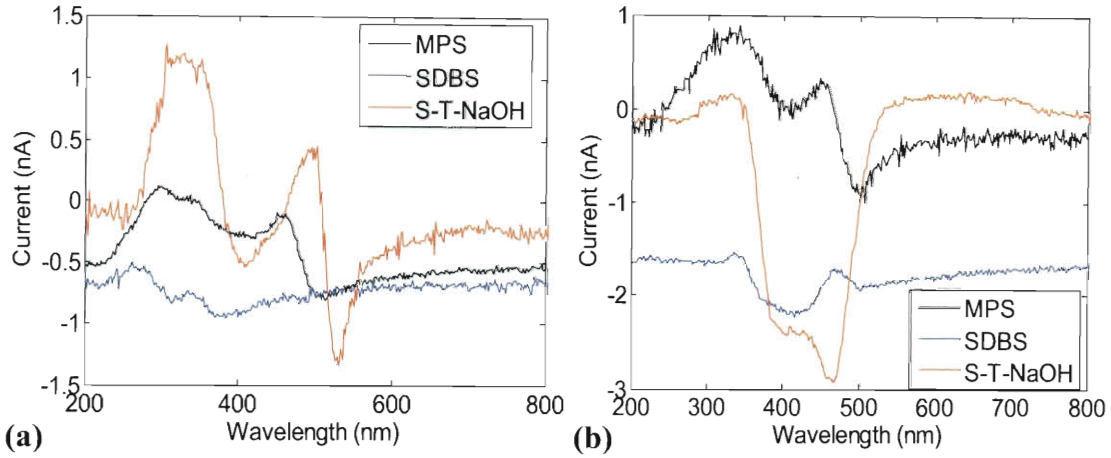

Fig. 3.12 Photocurrent from front-lit yellow CdSe tetrapod samples on ITO substrate vs. wavelength. Without (a) and with top gold layer (b) are shown. The counter electrode is ITO.

For longest red tetrapods (with arm about 40 nm), they have more chances to protrude tips after 10 nm gold sputtering, and act like antennae. The surface plasmon resonance is strongly dependent on the shape of the materials. In this case, we would have not only gold thin film but also nanowire-like spikes and some irregular shapes due to the protruding parts of the aggregates. Therefore, the current response became more complicated. To confirm this hypothesis, we need to do electrochemical analysis to determine the interaction of electrolytes and the gold surface, which will be described in the Chapter 4.

3.2.3 CdSe Tetrapods on Si/Pt/Au Surface

Since the ITO surface was too rough to be imaged under AFM, we changed to silicon substrate to characterize the samples. The tetrapods concentration we used here was 20 folds diluted with 30 second sonication (20x30s) in order to disperse tetrapods and form antenna arrays. All the samples gave increasing current with time once being illuminated. We determined it as baseline shifting rather than actual current responses, and thus normalized all the figures. However, during the intervals when we changed the high-pass filters and gratings (under illumination), the shifting would cause discontinuity in the photocurrent response. By normalization, it is easier to analyze the significant peaks, but also conceals or even modifies those small peaks. For this concern, we also did the white light tests by chopping the light on and off, and compared the results with wavelength scan to see if there is any inconsistence.

The photocurrent response from the tetrapods is largely decreased because of the diluted concentration. We can still see (negative) current appearing at absorbance peaks without top gold layer, but the amplitudes are much less than that with non-diluted concentration in the ITO substrate tests (Section 3.2.2). Moreover, after adding the gold layer, the effect of tetrapods became more insignificant and was hardly observed from the current responses. An interesting observation is that, without top gold layer, the tetrapods ehhibited two trends while directly exposed to the light. For short ones, namely black and yellow tetrapods with 12.5 nm in length, the photocurrent displayed the addition of the bandgap absorption of tetrapods on the blank samples (Fig 3.13 (b) and (d)). However, for longer red tetrapods with 40 nm in length, the photocurrent not only showed the addition of the tetrapods absorption but also a strong positive peak at 300 nm, which is about 1-2 nA (Fig 3.13 (c)).

In addition, after adding the top gold layer, for those samples in thiol solutions, especially for MPS, the current had a huge response at 300 nm (3-4 nA for red and yellow tetrapods, and 1.2 nA for black ones). An assumption is the well-organized SAM

of MPS on the gold arrays constructed on tetrapods support and rectified the current successfully.

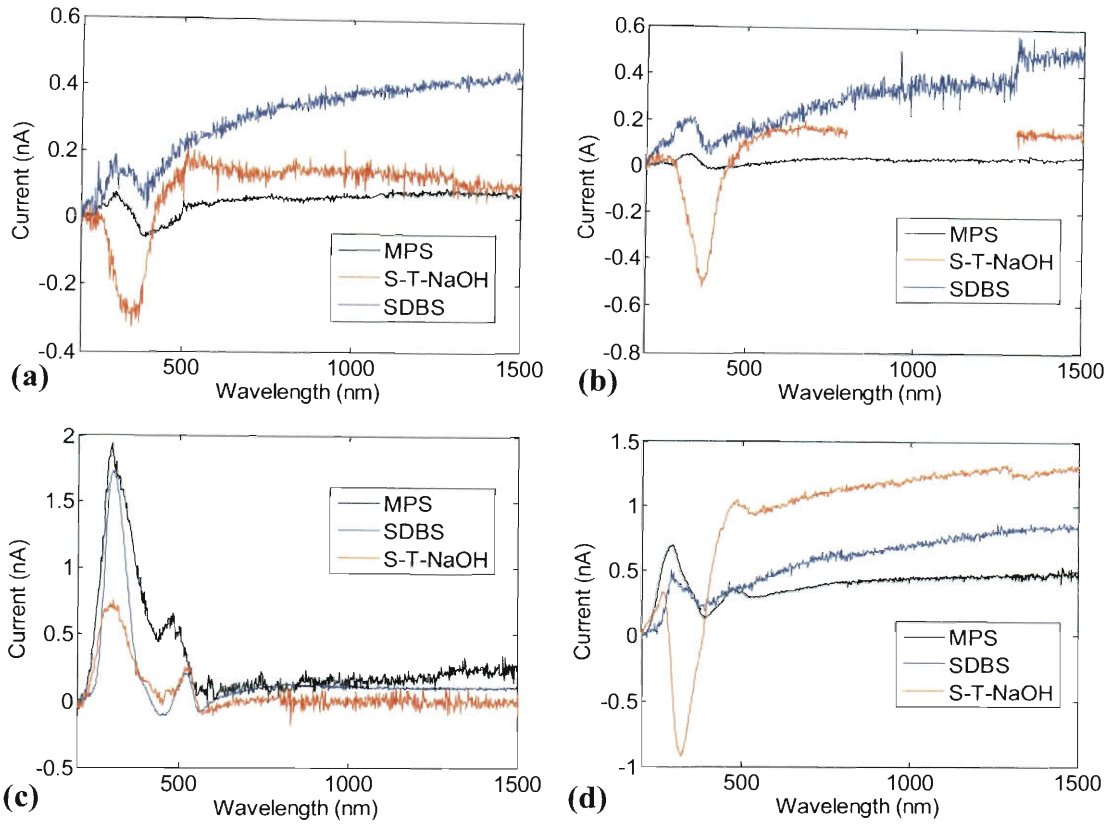

Fig. 3.13 Wavelength scans on the Si/Pt/Au surface with 20x diluted and 30 s sonication CdSe samples. (a) Control, (b) black, (c) red, and (d) yellow tetrapods.

3.2.4 Conclusions

We tried to fabricate gold as optical rectennae by sputtering a layer of gold on tetrapods support. However, the concentrations of the tetrapods are too high to disperse sparsely as antennae. Tetrapods act like thin film more than individual standing on the substrate with their top arms as vertical arrays. After replacing the substrate from ITO to silicon-based wafer, we also tried to dilute the concentration of tetrapods to construct vertical arrays.

The tetrapods-Au photovoltaic cells mainly display the characterization of bandgap absorption. The photocurrent responses mostly depend on the absorbance of the CdSe tetrapods, especially in the samples fabricated by non-diluted CdSe solutions. The organic self-assembled monolayer formations of the surfactant on tetradpods and ITO surface, and thiols on gold gave complicated photocurrent response, indicating multi mechanisms inside the system.

The possible reasons that the optical rectennae idea does not demonstrate well in these tests could be: (a) The aggregation of CdSe tetrapods is crucial that no efficient antennae were actually formed. (b) The lengths of the tetrapods are only 12.5 nm or 40 nm. Even if we consider the image charge appearing in the bottom conducting layer, and slower group velocity inside the gold compared to the speed of light, we are still hard to make those gold-coated tetrapods resonate with visible light but in the UV region instead. (c) The interactions between the materials are complicated and cannot be figured out only by measuring the photocurrent. Electrochemical or spectroscopic equipments are essential to uncover the mechanism. Another simplification is to reduce the kinds of the reactants. Therefore, we thought of constructing gold antennae array directly by growing gold nanowires through membrane templates. Therefore, gold become the only participant for us to examine the optical rectennae behavior.

3.3 Gold Nanowires Through Membranes

3.3.1 Length and Density Control of Gold Nanowires

The images were taken by scanning electron microscopy (SEM, FEI Quanta 400 ESEM FEG with beam energy of 25 kV and spot size of 3.0). The membranes are only 6 μm thick so that they are easy to flip or fold in the methyl chloride during the dissolution step. We have tried different means to affix them on several substrates. Silver paints and carbon tapes on ITO glass or silicon wafers have been tried, but both gave bad attachments and poor nanowire densities with side products. Finally we successfully

electroplated copper with several tens of micrometers on the sputtered gold at the bottom, which served as enhanced mechanical support of the membrane as well as the attachment to the silicon wafer base. The resulting nanowires density is significantly improved by adding a copper layer at the back (Fig 3.14).

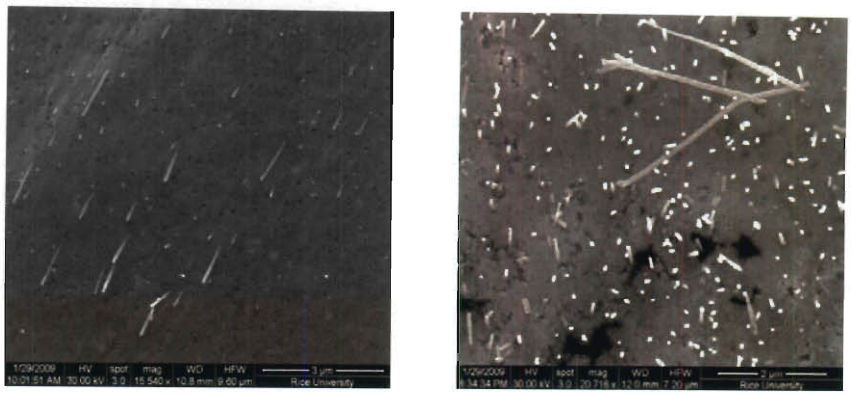

Fig. 3.14 Different densities of gold nanowires without (left) and with (right) copper electroplated at the bottom. The thickness of copper layer is about 15μm, and gold electroplating condition is 40 mM $HAuCl_4$ at 0.3 V for 1 minute. Significant enhanced density of nanowires is obtained with the copper layer.

Chloroauric acid ($HAuCl_4$) dissolved in water has been employed. We started from 10 mM (1.97g of Au/L) referred to papers [106, 107], which is also on the same order of the Orotemp 24 gold electroplating solution (8.2 g of Au/L). And we found that most pores were not filled (<20 %). In addition, typical deposition rate is about several hundred of nanometers per minute. But our deposition rates were over 2 μm per minute, resulting in long nanowires (>2 μm) in one minute or less. Moreover, most of them could not stand on the substrate and some had kinks, indicating their loose structures.

We varied the concentration of $HAuCl_4$, as well as the deposition voltage and time. The concentrations of 40 mM and 50 mM were also been tried. The voltage was varied from 0.3 V to 1.2 V, and the deposition time was altered from 30 seconds to 2 minutes. The yield was improved (>60 % pores were filled) by increasing the concentration of $HAuCl_4$, due to more ions depositing into the pores. Despite many so-called "cap"

structures were formed in all the samples implying that the gold nanowires grew beyond the membrane, we could not find any wires with 6 μm long (equals membrane thickness). This result confirmed that most wires had loose structure and thus broke into shorter ones.

It is worth noting that the problem we faced about using chloroauric acid is that we were unable to form nanowires with short and uniformly distributed length. The typical nanowires we obtained were mostly 2 μm long and some about 800 nm long. This non-uniformity could not be improved by changing the voltage or deposition time. Higher deposition voltages ended in more long wires (~70 %) while lower voltages gave less (~50 %) ones. No significant difference appeared by varying the deposition times. Figure 3.15 shows images of caps, long and short wires we have obtained in the process.

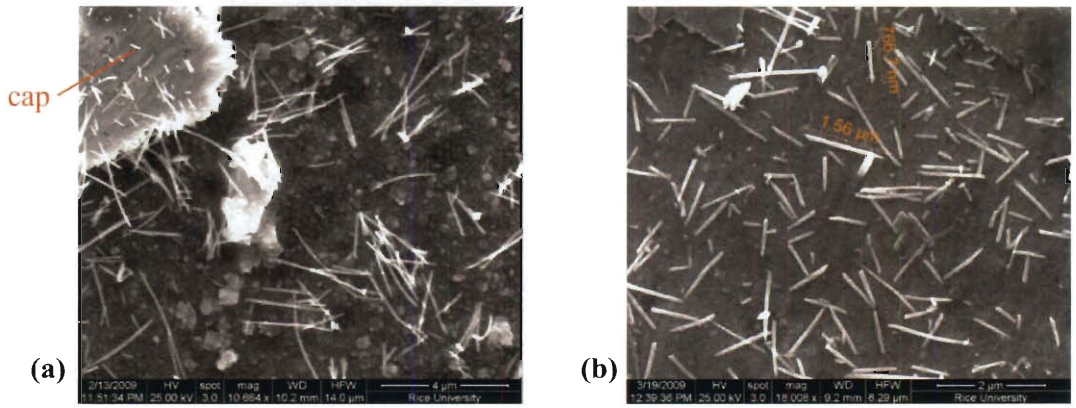

Fig. 3.15 Gold nanowires depositing from $HAuCl_4$: (a) "Cap" and long wires showing the fast growth rate and loose structure. (b) Short wires with average length of 800 nm lying on instead of protruding out of the substrate.

Furthermore, antennae are very sensitive to the direction with respect to the incident electromagnetic waves. The longitudinal direction of the wires needs to be parallel with that of the electric fields in the incident EM waves to successfully induce the surface plasmon resonance. Hence, we need to grow nanowire arrays with unitary direction, which are standing but not lying on the surface. Since the aimed aspect ratio of our nanowires is very big (L/D = 500 nm to 30 nm = ~17), that makes the wires very skinny and require more strength to stand freely. Unfortunately, $HAuCl_4$ did not give us good

results. The fast growth rate and poor attachment of the wires to the bottom sputtered gold layer make it harder to meet the expectations. In addition, if the wires were lying on the surface, then the SAM assembly may not cover all the surface area and construct incomplete barrier.

3.3.2 Photocurrent Response

The absorbed wavelengths of surface plasmon resonance of gold nanowires have two peaks. One is around 530 nm due to the transverse direction of the wires, and the other due to the longitudinal direction lies within the region of 500-1000 nm depending on the aspect ratio of the gold nanowires [68, 108]. By switching the light on and off, the current responses were recorded under white light and light beyond 455 nm (each cycle ~60 seconds). The positive and negative spikes may due to three factors, the charging and discharging at the interface of gold-thiol monolayer and electrolyte solution [109, 110], the corrosion between the working electrode and counter electrode, and the imperfect SAM around the nanowires. Note that three continuous tests using the filter (purple boxes, Fig. 3.16) showed very stable saturated current about 0.6 nA induced by the gold nanowires under illumination. From photocurrent responses under white light (orange boxes, Fig. 3.16), we could see some currents contributed by the wavelength below 455 nm from its saturated current (0.8 nA). It could be accidental illumination on the ITO as we discovered in the tetrapods experiments as well.

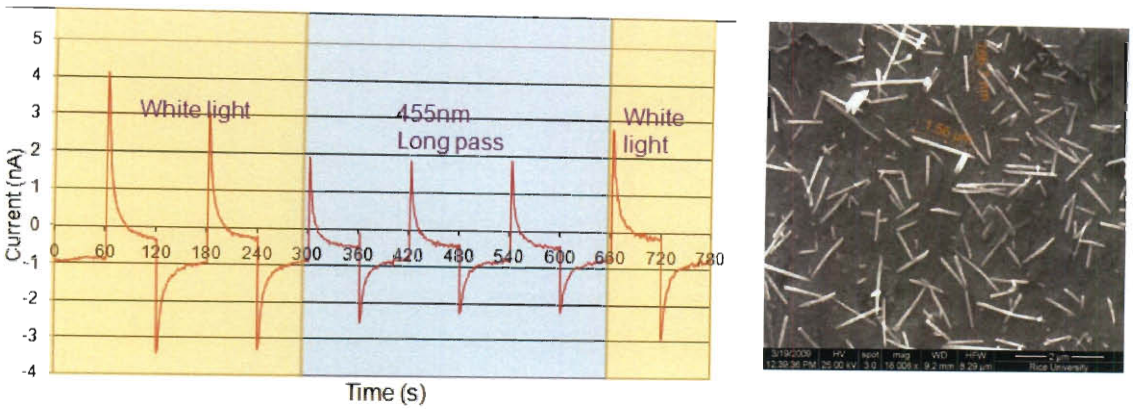

Fig. 3.16 White light and 455 nm cut-off light as a function of time by chopping the light on and off, each period for 60 sec. On the right shows the SEM images of the sample. The electrolyte was S-T-NaOH. Electroplating condition was 50 mM HAuCl4 at 3.5 V for 10 sec and 0.5 V for 15 sec. Note that the growth rate was high that most wires were lying on the substrate.

Figure 3.17 shows a representative photocurrent response as a function of wavelength of gold nanowires immersed in S-T-NaOH electrolyte. A control without nanowires containing only carbon tape (blue trace, Fig. 3.17 (a)) shows no current, indisputably tells that photocurrent can be generated from 380-800 nm by gold nanowires (green trace, Fig 3.17 (a)). Note that the nanowires were sit on a 100 nm-thick gold thin film, and therefore the first current response at 400 nm could due to the SPR of gold thin film [65]. The second peak is a broad current response from 500 to 800 nm. This is a combination of the SPR of gold thin film and nanowires with different length. Evans *et al.* found that the larger absorbance peak would blue shift with smaller aspect ratios of gold nanowires, and merge with smaller absorbance peak when aspect ratio is twelve [108]. For those short wires, the average length is about 600 nm, which gives the aspect ratio about 12. The broad peak from 500-550 nm is caused by those wires, which is consistent with their finding. Despite we only generated small current, SEM images (Fig (3.17 (b)) showed that most wires were entangled with several micrometers in length, which cannot be used as rectennae in visible region.

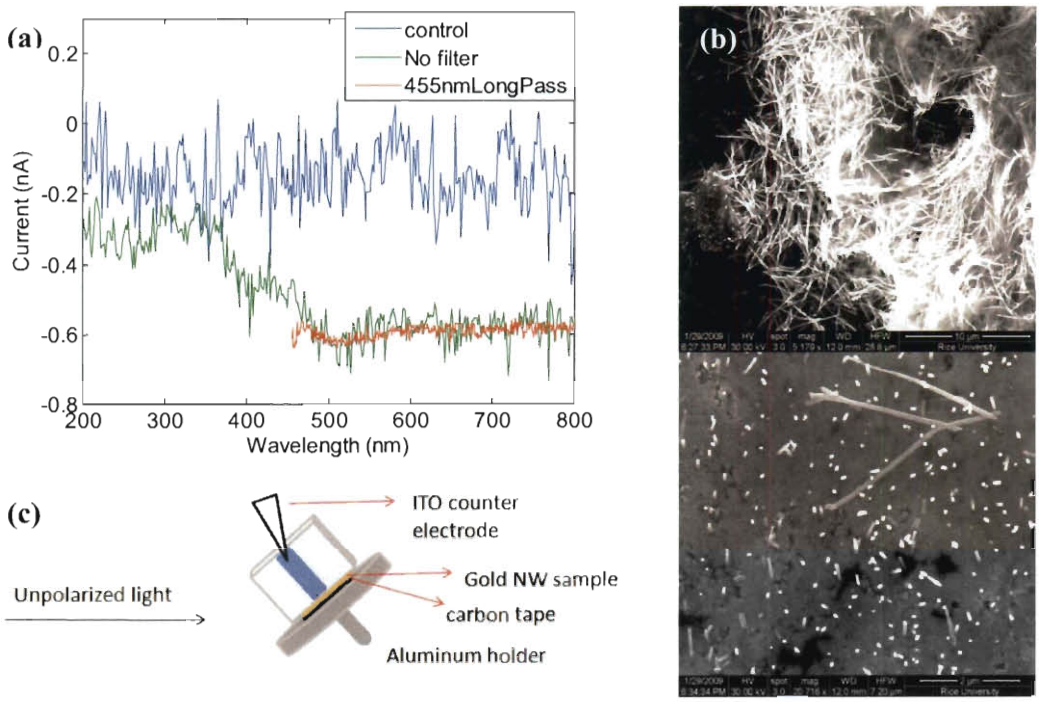

Fig. 3.17 Photocurrent as a function of wavelength of gold nanowires. (a) Broad peak at 500-550 nm was observed. The red trace, which is under filtered light, also confirmed the peak. (b) SEM images of the sample, showing large portion of entangled long nanowires, and small portion of standing wires with ~600 nm in length. (c) Experiment setup. The electroplating condition was 40 mM $HAuCl_4$ at 0.3 V for 1 min.

3.3.3 Conclusions

Our electroplating process of obtaining gold nanowires through polycarbonate membrane is still not mature with $HAuCl_4$ as electroplating solution. It gave us loose wires with non-uniformly distributed length and density. The photocurrent that was generated from the gold nanowires is on the order of 0.1 nA, indicating the imperfect conditions of gold nanowires. Surface plasmon resonance of nanowires was observed in samples, but in general, the current was very low. The reasons may due to the undesired length of gold nanowires, as well as loose construction of SAM as rectifying barrier. An important observation is that the current flow was opposite from which declared in out

hypothesis. The rectification should exist due to the generated current, however, we need to verify and modify our assumptions.

Since SAM is a critical element in the system, we should explore more about the characterization of SAM on the gold nanowires. In the next chapter, we identify the tunneling barrier constructed by alkanethiolates on gold nanowire structures.

CHAPTER 4

Characterization of the Tunneling Barrier of SAM on Gold Structures

From the preliminary results, we need further investigation to characterize the SAM formation on gold nanowires. Surprisingly, lots of efforts have been put into the SAM on thiolated gold nanoparticles and films, but only mere attention have been paid to thiolated gold nanowires. In order to figure out the appropriate SAM for photovoltaic use, we need to know the tunneling properties of the gold nanowire arrays built on gold films. Note that the nanowires were grown on a bottom gold film, thus SAM would be formed on the nanowire arrays and also on the bottom gold film. To get the information from pure nanowire arrays, as shown in Fig. 4.1, we need to substrate the signal from the pure gold film from that of nanowire arrays on gold film (will be annotated as film + NW in the rest paragraphs). By using the electrochemical methods, we derive the tunneling barrier coefficient (β) for different thiolated gold nanowire-film samples.

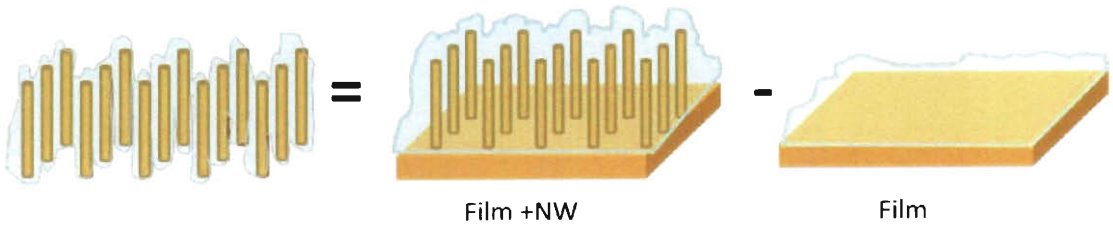

Fig. 4.1 Scheme of obtaining pure information from gold nanowire arrays. The pink shadow indicates the SAM formation.

4.1 Experimental

4.1.1 Sample Preparations

All the chemicals were purchased from Sigma-Aldrich. The alkyl thiols $HS(CH_2)_xCOOH$ (x = 2, 7, and 11) were received as powder and prepared for 1 mM in 200 proof ethanol solution. The samples will be annotated as SC3OOH, SC8OOH and SC12OOH in the results part. $HS(CH_2)_xCOOH$ (x = 10 and 15) were purchased as 5 mM ethanolic solution and diluted to 1 mM with 200 proof ethanol. The commercial solution will be annotated as NT11 and NT16 in the results.

For self-assembly, the substrates were fabricated on a silicon wafer sputtered with 200 nm Au. A 7 nm Cr layer was deposited as adhesion layer prior to the Au deposition. For film samples, the substrates were rinsed with ethanol before immersed in the 1 mM thiols for 40 h. For film + NW samples, the nanowires were grown by template synthesis. The gold electroplating solution (Orotemp 24 purchased from Technic Inc.) was reduced to gold and deposited through anodic aluminum oxide (AAO) nanoporous membrane with a pore size of 200 nm. The applied voltage was -0.9 V with respect to the Ag/AgCl reference electrode, and the electroplating time was 10 min. After the nanowire growth, the sample was attached to a silicon substrate top-sputtered with 100 nm Au by gluing silver paint at the side of the membrane. The membrane was later dissolved in 3 M NaOH and resulted in free-standing nanowires. The procedure is illustrated in Fig. 4.2. The free-standing nanowire samples were rinsed with water and ethanol prior to the SAM formation. The immersion time for film + NW samples was 48 h because of a longer diffusion time for dense array structures.

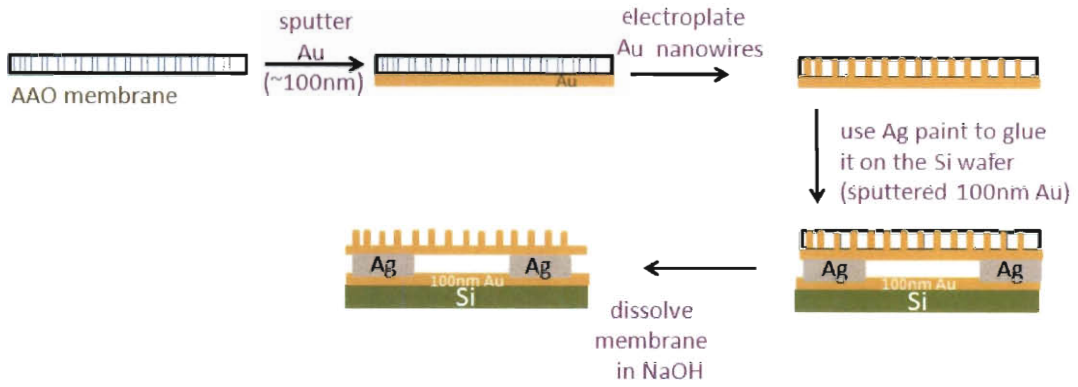

Fig. 4.2 Procedure to obtain free-standing gold nanowire arrays.

4.1.2 Ellipsometric Thickness Measurement

The thicknesses of the films were determined by ellipsometry using Stokes Ellipsometer LSE from Gaertner Scientific Corporation. The ellipsometer determines the complete polarization state of the 632.8 nm laser measuring beam at a 70° incidence angle. Immediately after the last sputtering deposition, the complex refractive index was measured. After the SAM formation, the samples were rinsed with ethanol and dried by a N_2 stream prior to the thickness measurement. The real refractive index is set at 1.45, and the thickness is measured by fitting the model with the previous values for bare samples. For the film + NW samples, we cannot measure the thickness directly from the nanowire structure because of the fitting model. Therefore, we measured the thickness of the film that lies next to the NW area.

4.1.3 Electrochemical Analysis

Cyclic voltammetry (CV) and electrochemical impedance spectroscopy (EIS) were performed with a three-electrode potentiostat (Gamry reference 600) to investigate the electrochemical properties of the SAM on gold nanostructures. A Ag/AgCl was used as reference electrode and a platinum rod as counter electrode. The samples were washed with ethanol and dried by N_2 stream before the measurement. The CV was performed between -0.2 V to 0.6 V with the scan rate as 50 mV/s. The electrolyte was 2 mM of

potassium hexacyanoferrate(II) trihydrate and potassium ferricyanide(III) (both from Sigma-Aldrich) in 0.1 M KCl solution. For the EIS measurements, a sine wave with amplitude 10 mV was applied to the system at the open circuit voltage, when and frequency varied from 10 mHz to 50 kHz. The results were analyzed and modeled using a complex nonlinear least squares (CNLS) fitting by EChem Analyst software from Gamry Instruments.

4.2 Tunneling Barrier of SAM on Gold Film

4.2.1 Thickness

The thickness of the gold film is measured by an ellipsometer. Fig 4.3 (a) shows the ellipsometric thickness of mercaptocarboxylic acids as a function of the chain length. For short chain thiol, e.g. n equals 2 and 8, the thickness is not consistent between the two samples which were immersed in the same batch of thiol solution. This is in agreement with the statement that shorter chain monolayers have more defect structures with lower packing density and coverage [111]. With increasing chain length, the stability of the formed monolayers increases and a linear growth in thickness with respect to the number of methyl groups is observed. Linear regression leads to a slope of 1.08 Å and a y-intercept of 4.15 Å. The data is in agreement with the theoretical estimated slope of 1.16 Å for each methyl group when the chains are 30 degree tilted from the surface [112]. The slightly shorter length for each additional methyl group can be explained by a more stressed and compact structure of monolayers on the gold film. Table 4.1 shows the values calculated using the regression equation and the theoretically expected thicknesses according to the literature. The errors are less than 10 %.

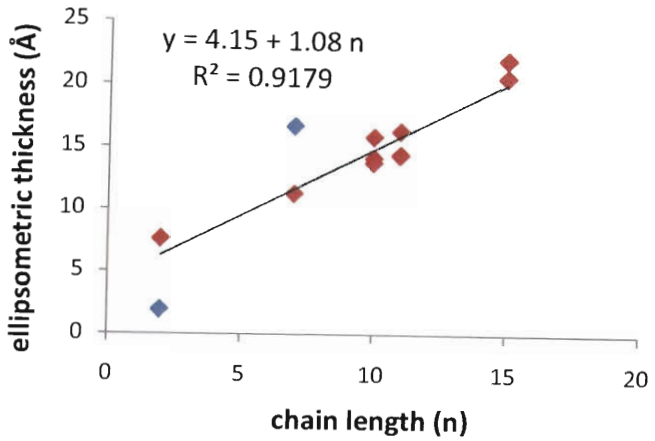

Fig. 4.3 Ellipsometric thickness of mercaptocarboxylic acids, $HS(CH_2)_nCOOH$, on gold film. The regression line indicates the expected thickness for different chain lengths.

TABLE 4.1 Comparison of the calculated thickness from the data shown in (a) and the literature [112].

chain length (n)	thickness (Å)	thickness (Å)
		Bain et al
2	7.38	7.12
7	11.69	12.92
10	14.93	16.40
11	16.00	17.56
15	20.32	22.20

4.2.2 Cyclic Voltammetry

The cyclic voltammetry and electrochemical impedance measurement were performed to derive the tunneling properties of SAM on gold films. For bare gold sample (black trace in Fig. 4.4), the characteristic waves with two reversible peaks at around 350 mV and 50 mV represented the cathodic and anodic current for $Fe(CN)_6^{3-/4-}$, respectively. The current was decreased dramatically with increasing chain length. For any n higher than 7, the current was rapidly reduced. For longer chain lengths (n > 10),

the current was further suppressed to absolute values of less than 5 nA, indicating well-defined and dense packing and consequently better blocking properties.

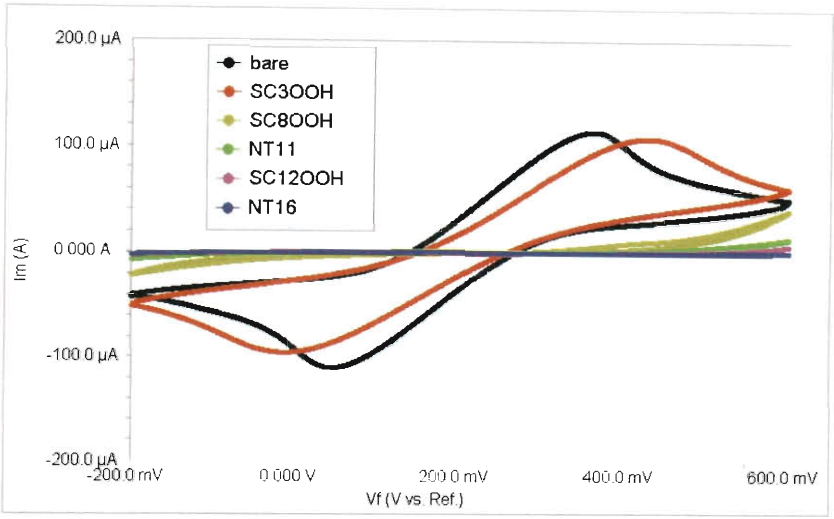

Fig. 4.4 Cyclic voltammogram of alkanethiols on gold films. SC3OOH, SC8OOH, NT11, SC12OOH and NT16 represents the thiolates $HS(CH_2)_nCOOH$, with n = 2, 7, 10, 11, and 15, respectively.

4.2.3 Equivalent Circuit and Tunneling Coefficient Calculation

To analyze the data obtained from the electrochemical impedance spectroscopy, we used various equivalent circuits to describe the processes taking place in the system. The Randles cell is shown in Fig. 4.5 (b), consisting of a solution resistance (R_s), a charge-transfer resistance (R_{ct}), a double layer capacitance (C_{dl}) and a frequency-dependent Warburg impedance (W). If the diffusion step is not significant, the Warburg impedance can be ignored and the Randles cell can be simplified as shown in Fig. 4.5 (a). It can also split the Warburg impedance into a constant phase element (CPE) in parallel with a diffusion resistance (R_{diff}) as in Fig. 4.5 (c).[113] The CPE considers the non ideal capacitive response of the interface. The impedance of the CPE is expressed as

$$Z_Q = \frac{1}{Y_0(j\omega)^{\alpha}}, \tag{4.1}$$

where Y_0 is a proportionality constant which contains the diffusion coefficient and other parameters regarding the electrochemical system, ω is the angular frequency, and α is an exponent ($-1 \leq \alpha \leq 1$). For $\alpha = 1$, the CPE has pure capacitive behavior. We used these three models to fit the data, and extracted the number from the best fit model. Figure 4.6 shows an example of EIS fitting for HSC_2COOH with well-fitted curves compared to the data.

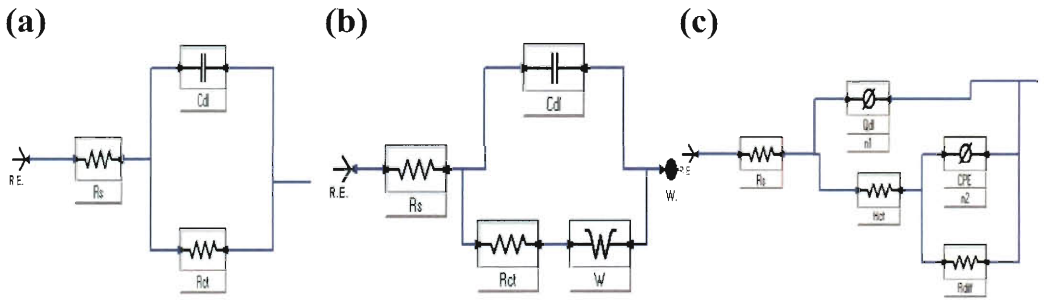

Fig. 4.5 Three equivalent models used for the ac impedance data: (a) simple cell, (b) Randles cell and (c) complex cell adapted from Ref [113].

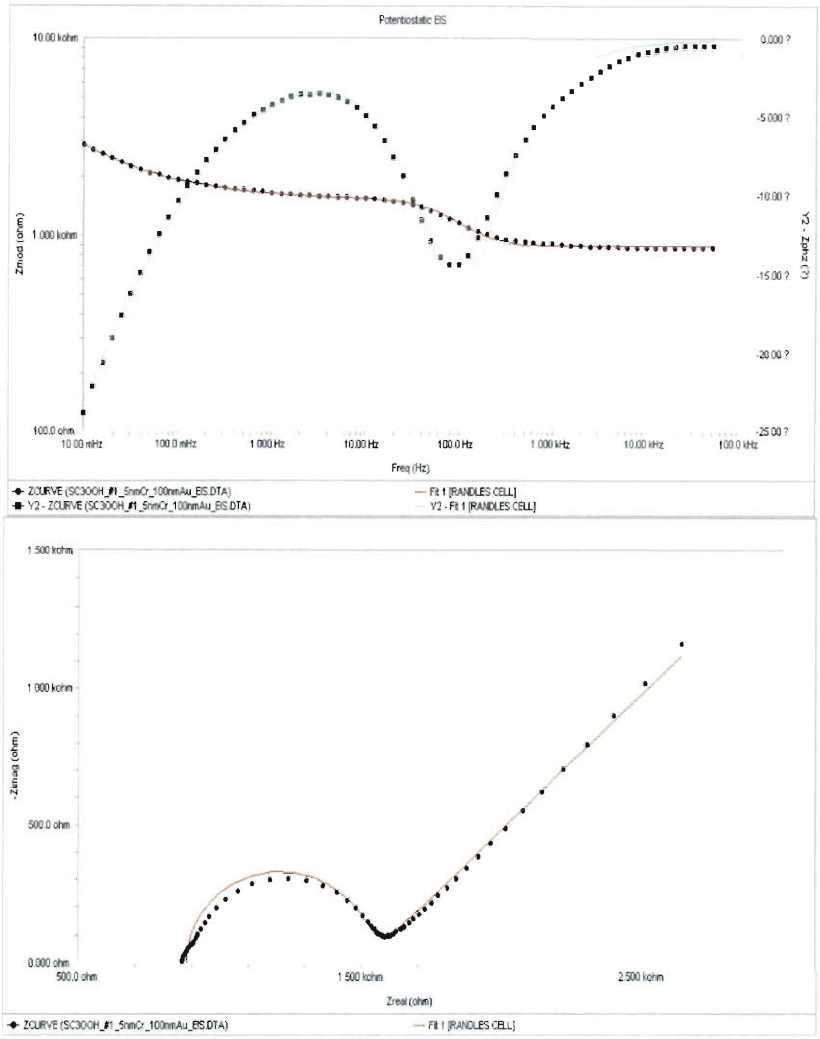

Fig. 4.6 EIS model fitting of (a) Bode plot and (b) Nyquist plot for HSC_2COOH.

The value of R_s is almost constant (around 900 Ω) for all samples because it is only dependent on the resistance of the solution and the distance between the electrodes, which is kept constant for all tests. The charge transfer resistance (R_{ct}) is affected by the thickness of the blocking monolayer, i.e. the chain length. It represents the electron transfer rate of the redox probe at the interface and is determined by the diameter of the semicircle appeared in the Nyquist plot. Figure 4.7 plots the R_{ct} as a function of chain length. The charge transfer resistance increases with the increasing chain length because of the thicker monolayers which suppress the tunneling of the redox probe through it.

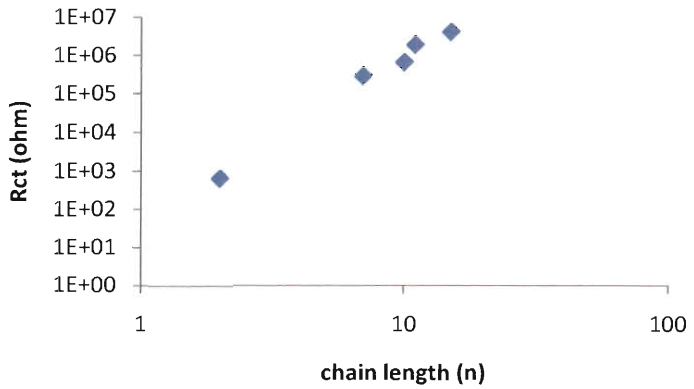

Fig. 4.7 Charge transfer resistance as a function of chain length.

By using the value of R_{ct} in Eq. (3.7), we can calculate the heterogeneous charge transfer coefficient k_{et} with k_0 as 0.031 cm/s for bare gold films, and furthermore, extract the tunneling coefficient β by inserting k_{et} into Eq. (3.8). β has been calculated to be 1.02 $Å^{-1}$ per CH_2 for $–CH_3$ terminal group [73]. For carboxylic terminal group, Cecchet *et al.* has reported that β is 0.5 $Å^{-1}$ for $HSC_{10}COOH$ on gold films by assuming the average length as 22 Å [114]. They also pointed out that β lies between 0.8 and 1.5 $Å^{-1}$ for saturated chains, while it is between 0.2 and 0.6 $Å^{-1}$ for unsaturated chains. Figure 4.8 shows the value of β per methyl group as a function of the chain length, calculated from both the measured thickness and the theoretical thickness. Ideally, β should be independent of the chain length after normalization. However, the shortest and longest chain (n = 2 and 15) show different values compared to the other three thiolates. For the three thiolates with n being 7, 10 and 11, the β value is about 0.37 $Å^{-1}$ for the measured thickness and 0.30 $Å^{-1}$ for the theoretical one. The smaller value compared to 1.02 $Å^{-1}$ for $–CH_3$ might due to the repulsive forces among unsaturated ionized $-COO^-$ terminal groups which results in defects.

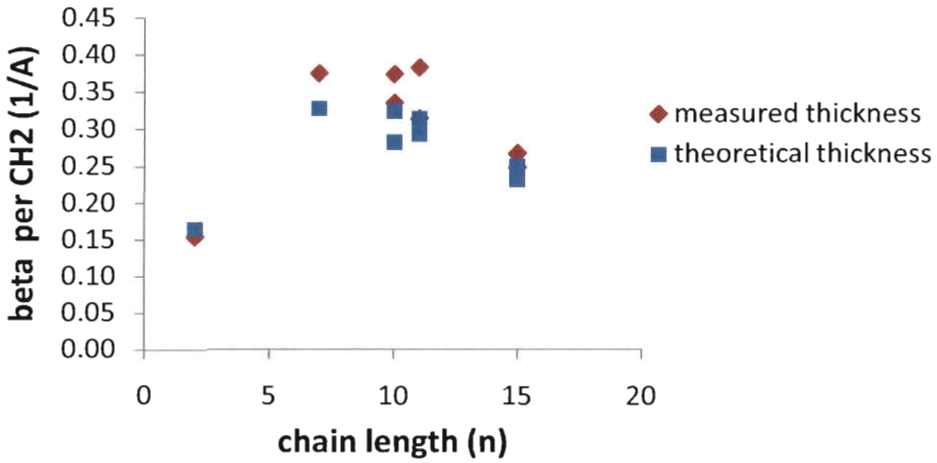

Fig. 4.8 Tunneling coefficient as a function of chain length for SAM on gold film.

4.3 Tunneling Barrier on SAM on Gold Film + NW Structures

4.3.1 Morphology and Thickness

The morphology of gold nanowires was examined by a scanning electron microscope (SEM). Since the pore density of AAO membranes is very high (10^{12} pores/cm^2), the nanowire arrays exhibit very dense packing as shown in Fig. 4.9 (a). The wires bundled to several forests because of the capillary force present during the drying process. This lowers the ability of the thiols to self-assemble because the nanowires are not individually separated from each other. The side view (Fig. 4.9 (b)) shows the bottom gold film (~100nm thick) and roughly 1μm long gold nanowires. Fig 4.9 (c) shows an actual diameter of the gold nanowires of almost 300 nm. This results in an aspect ratio of about 3.

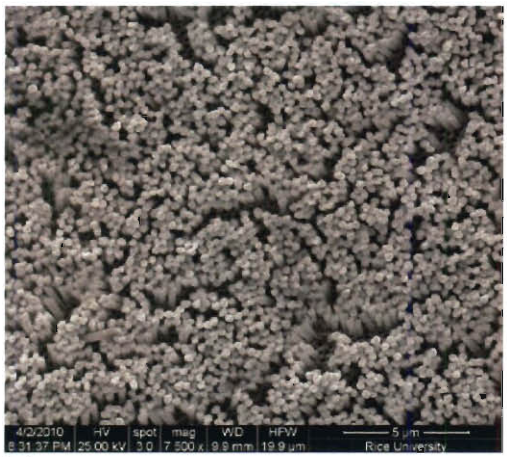

(a)

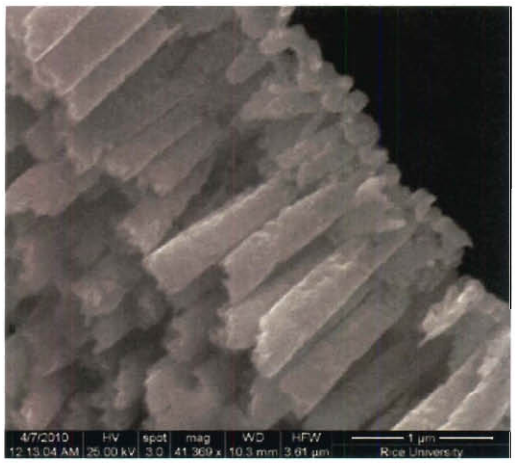

(b)

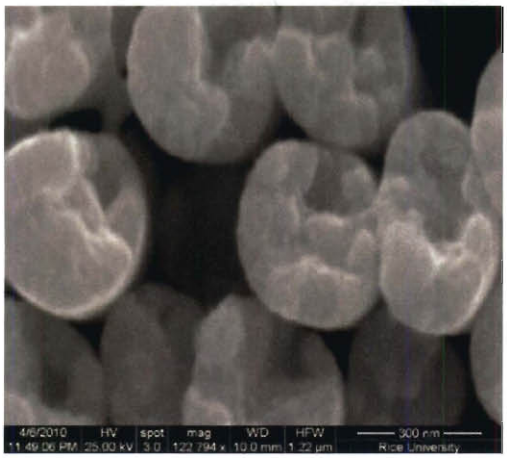

(c)

Fig. 4.9 The morphology of a gold nanowire array. (a) Top view, (b) side view and (c) higher magnification on the topographic structure.

Though the electroplating is a convenient method to produce nanowire structures in a controllable way, the amount of defects present among the nanowires is not satisfying. Figure 4.10 shows two images illustrating defects formed during the growing process. Figure 4.10 (a) shows hollow structures occurred at the edge of the electroplating area. Those defects were formed because that the electroplating solution didn't efficiently diffuse through and fill the pores. Figure 4.10 (b) shows the combination of the colloid

particles and rigid rod deposition. The bottom of the nanowires is loose-structured, while more rigid structures appeared at the top. The loose structure can break the nanowires from the bottom, and block the electron transfer along the nanowires.

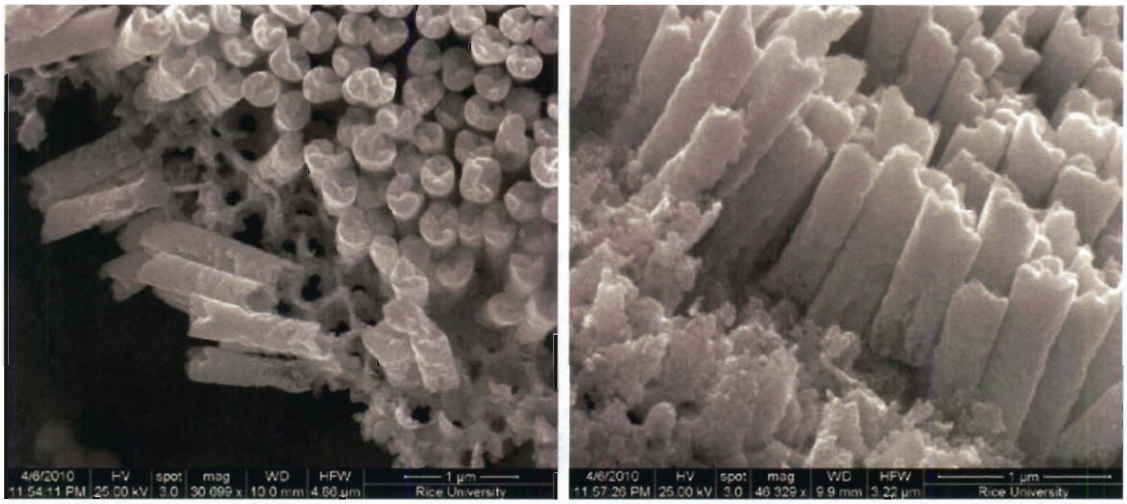

Fig. 4.10 Defects in the nanowire samples. (a) Hollow structure and (b) Loose attachment to the bottom gold film.

Since only three thiolates exhibit a consistent tunneling coefficient, we tested the SAM on gold film + NW samples with the particular thiols (n = 7, 10 and 11). The thicknesses of the film + NW samples were measured on the pure film area which is next to the NW area on the same piece. Table 4.2 shows the thickness of the film and the film + NW samples as well as the theoretically expected values. All three kinds of thiols show thicker formations than the ones present on the gold film (Table 4.1). It implies that multilayers or entangled structures might be formed because of the unclean gold surfaces. In fact, the samples were immersed first in the electroplating solution (Orotemp 24) for 20 min and then in concentrated 3 M NaOH for three hours, which most likely caused the contamination of the substrates which is not washed off completely.

TABLE 4.2 Comparison of the thickness among the film + NW, film and theoretical values for HSCnCOOH (n = 7, 10 and 11).

	Film + NW (Å)	**Film (Å)**	**Theoretical (Å)**
SC8OOH	15.51	11.31	12.92
NT11	19.02	15.94	16.40
SC12OOH	22.45	16.42	17.56

4.3.2 Bare Samples Comparison

This section compares the CV and EIS of bare gold film and film + NW sample. Figure 4.11(a) shows the cyclic voltammogram of two bare samples. The gold film exhibits reversible cathodic and anodic peaks, whereas the film + NW shows significantly higher peak currents and a capacitance curve at both ends of the scan range. The larger currents are explained by the larger surface of the gold electrode. The capacitance is caused by the less structured monolayer arrangement that delays the electron transfer and leads to a slower response to the voltage change during the potential sweep. The EIS data for both samples are mostly identical. Table 4.2 shows the values of the equivalent circuit elements of Randles cell. The solution resistance and Warburg impedance of the two samples coincide within a tolerance of 18 % and 4 %, respectively. The charge transfer resistance of gold film + NW is near twice smaller than that of gold film; the capacitance of the gold film is 20 times smaller than that of the film + NW. Both are in agreement with the cyclic voltammogram.

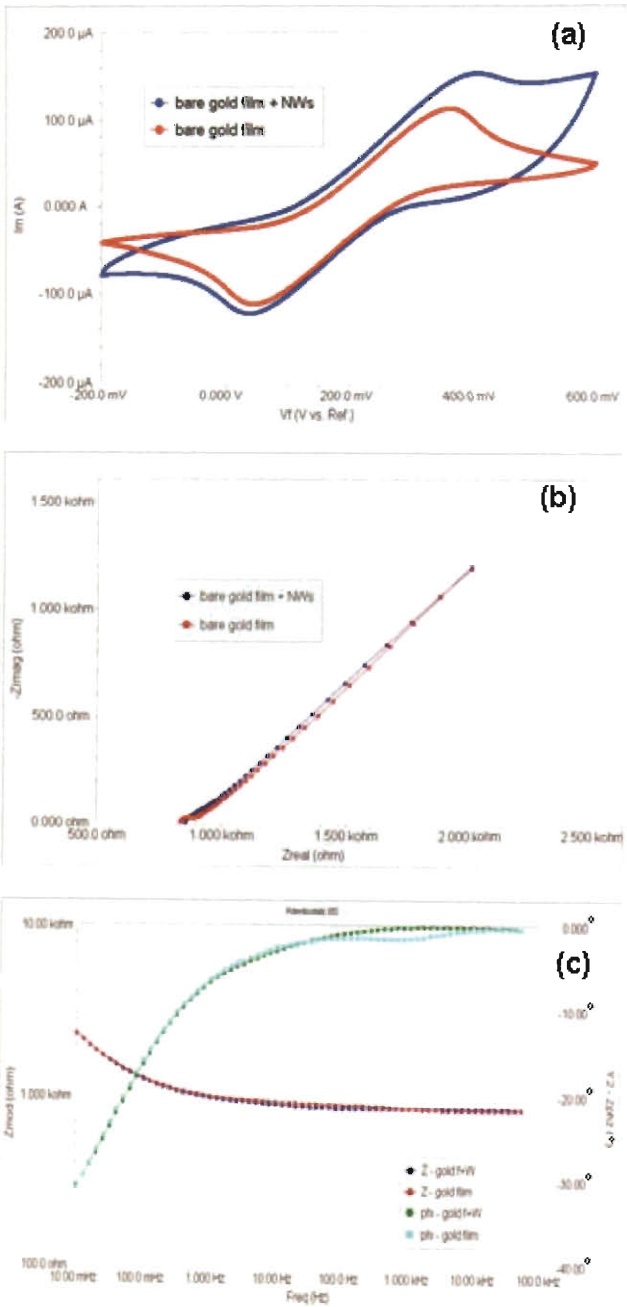

Fig. 4.11 Comparison of bare gold film samples and film + NW samples. (a) Cyclic voltammogram, (b) Nyquist plot and (c) Bode plot.

TABLE 4.3 Comparison of the EIS model fit of the gold film + NW with the film sample.

parameter	Gold film +NW	Gold film
R_s (Ω)	855.9	840.3
C_{dl} (F)	87.21 e-6	4.299 e-6
R_{ct} (Ω)	28.47	50.27
W ($S*s^{1/2}$)	2.473e-3	2.484e-3

4.3.3 Cyclic Voltammetry

The electron transfer from the electrolyte to the electrode is possible through three paths: (a) tunnel through the monolayer, (b) permeate through the monolayer and react at the electrode surface, and (c) diffuse to a pinhole or defect spot on the electrode [115]. Since there is no electroactive species present in the electrolyte, only path (a) and (c) are considered. The diffusion current time for path (c) is much higher than tunneling current, so a significant current can be observed if a pinhole or other defects are present on the electrode. The cyclic voltammograms of gold film + NW samples show that the faradaic current of all the samples are observable around the oxidation and the reduction potential of the redox probe. The reversible peak currents indicate that the blocking monolayer is not well-constructed on the electrode, which allows the electrons passing the interface by diffusing through the defects. Despite comparably short chain length, the commercially available solution NT11 shows the best blocking behavior among the three kinds of thiols. However, in general, the diffusion currents through defects are significantly higher than corresponding values for bare gold films.

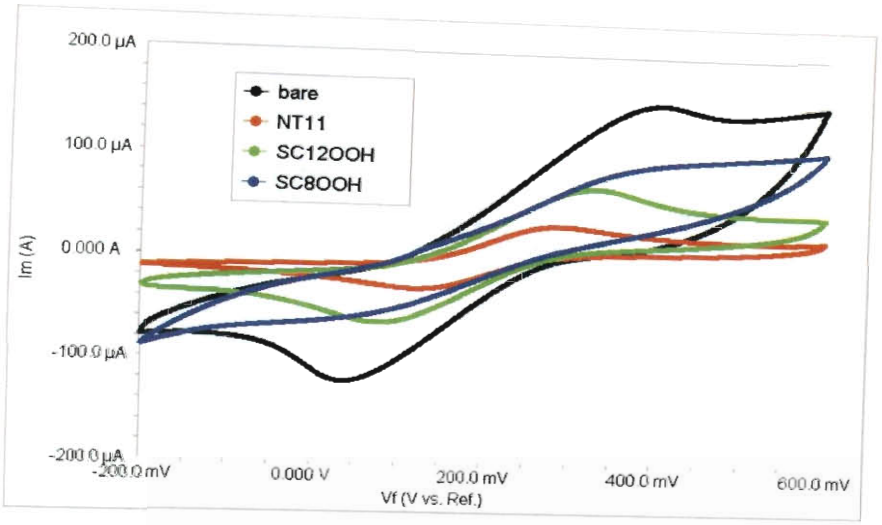

Fig. 4.12 Cyclic voltammogram of alkanethiols on gold film + NW samples.

4.3.4 Tunneling Coefficient and Potential Barrier Calculation

The tunneling coefficient was calculated for gold film + NW samples using the same modeling method as for the EIS data. From previous section, the tunneling coefficients of film samples were between 0.28 and 0.38 $Å^{-1}$. According to Fig 4.13, the β of film + NW samples are one order of magnitude lower. Several reasons may cause this difference. First, the gold nanowire arrays are not well-structured on the electroplating area, which may indicate defects on the sample. This prevents the thiols from self-assembly. In addition, the aggregates of arrays make it harder to form the SAM smoothly and homogeneously on the gold nanostructures. This also creates pinholes on the SAM formation easily. Furthermore, the external solvents used prior to the thiol immersion, e.g. Orotemp 24 for growing nanowires, and sodium hydroxide for dissolving the AAO membrane, can modify the chemical properties of the gold surface and cause the defective monolayer formation.

The charge transfer resistance of film + NW shows the opposite trend compared to films, i.e. the value of R_{ct} decreases slightly with increasing chain length, which indicates a faster electron transfer for longer chain length. This is in disagreement with the theory, which states that longer hydrocarbon chains have more tunneling resistance through the

blocking layer. Since the thickness of the thiols is higher than the theoretical values of about 4 to 5 Å, the possibility of forming multilayer at smaller chain lengths should be ignorable. However, because of the steric hindrance between the nanowires, it might be more difficult for longer chain lengths to diffuse through the array and self-assemble on the gold nanostructures. Thus, the tunneling coefficient would decrease due to more pinholes.

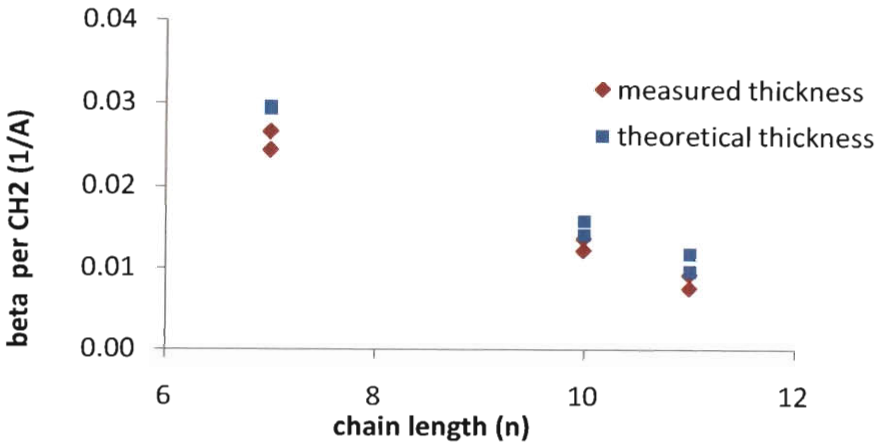

Fig. 4.13 Tunneling coefficient as a function of chain length.

The potential barrier (V) can be calculated from the equation $\beta = 1.025\ V^{1/2}$ (Eq. (3.6)). Figure 4.14 shows the potential barrier for both gold film and film + NW samples as a function of the chain length. For gold films, the potential barrier lies between 0.4 to 0.6 eV. This is in agreement with the calculation for ω-hydroxyl thiol ($HO(CH_2)_nSH$) by Miller *et al.* [116]. For film + NW samples, the potential barrier is comparably small. Comparing the calculated potential barriers to the thermal energy of 0.024 eV at 300 K shows that the two energies are in the same order. This leads to the conclusion that the potential barrier of the SAM on film + NW samples was not formed successfully to serve as blocking rectifier. The experiment has been performed when the circuit was not irradiated by light which may explain the failed potential barrier formation..

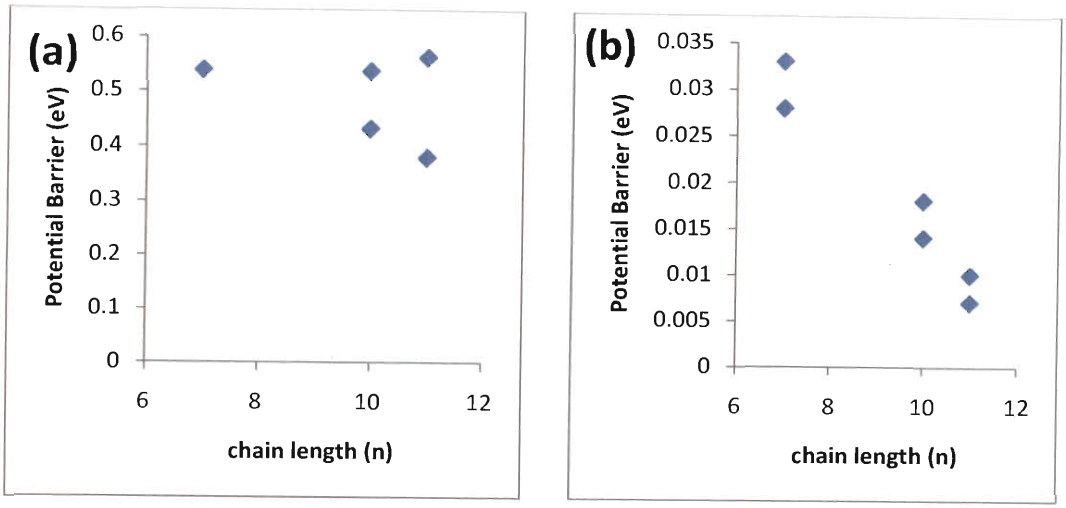

Fig. 4.14 Calculated potential barrier of (a) film and (b) film + NW samples as a function of chain length.

To further support the argument, we calculated the surface coverage (Θ) to be

$$\Theta = 1 - \frac{R_{ct,bare}}{R_{ct,SAM}}, \tag{4.2}$$

where $R_{ct,\,bare}$ is the charge transfer resistance for bare samples [78]. The charge transfer resistance is on the order of 10 Ω for bare films and on the order of 10^6 Ω for SAM-modified films. For film + NW samples, resistance is on the order of 10 Ω for the bare case but on the order of 10^2 Ω for SAM-modified film + NW samples. Therefore the surface coverage is 99.999 % for gold film but only 90 % for film + NW samples. The approximate 10 % difference in the amount of defects is significant and provides a reasonable explanation of the fact that only a leak current rather than a tunneling current is observed. As a result, the low tunneling coefficients for film + NW are obtained.

We also implemented the contact angle measurement to re-confirm the surface properties of the gold film prior to the thiol immersion. The contact angle for bare gold films is about 70° which is in agreement with the typical value. However, for bare film + NW samples, the two measurements resulted in angles of about 50° and less than 10°, inferring that a very hydrophilic surface is present. The AAO is very hydrophilic, so the

contact angle measurement indicates that there are still some AAO residues present, which block the gold from bonding to the sulfur atom and have defective SAM formation.

Surprisingly, the EIS data of film and film + NW show two completely different shapes, indicating different rate-limiting steps for two systems. For films, the impedance is on the order of 10^6 Ω and a large semicircle is formed for thiols longer than n = 2. For film + NW samples, the impedance is on the order of 10^3 Ω and the samples exhibit a much smaller semicircle with a long 45° tail at the lower frequency region. As addressed in Fig. 2.23, the semicircle represents the kinetic control, and the tail is for mass transfer control [77]. Therefore, the kinetic control dominates for film samples, whereas the mass transfer dominates in the flim + NW samples. Figure 4.15 shows representative Nyquist plots for $HSC_{10}COOH$ on film and film + NW sample.

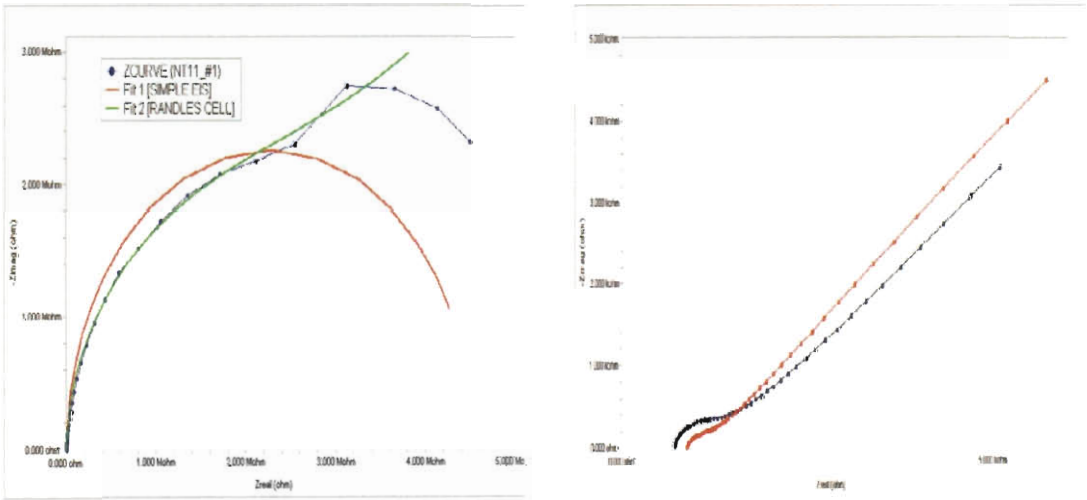

Fig. 4.15 Nyquist plots of HSC10COOH on (a) film and (b) film + NW samples.

4.4 Conclusions

The tunneling barrier properties of SAM on both gold film and gold film + NW structures were investigated. Two electrochemical analyses, i.e. cyclic voltammetry (CV) and electrochemical impedance spectroscopy (EIS), were performed to extract the tunneling coefficients. For SAM-modified films, the CV shape and EIS modeling results are in agreement with values stated in the literature. However, for the gold film + NW samples, the results differ from the corresponding values derived for gold films. Much smaller tunneling coefficients were obtained from those samples indicating defective SAM formation and very small rectifier barrier height.

One concern for the tunneling coefficient calculation is that we assume the SAM grows the same on either film or nanowires. Because of the complexity of building the ellipsometric model to calculate the thickness on the rod-like substrate, we measured the thickness on the film area which was next to nanowires area. This indirect measurement might overlook the possibility that the SAM grows differently within the space-restricted nanowire array from spacious film surface. However, from the contact angle measurement, we are certain that the coverage of SAM on film + NW is much poorer than that of film samples. Therefore, the tunneling coefficient of film + NW should still be smaller than film because of the pinholes. Further improvement on the better self-assembly of thiolates on gold nanowires is suggested.

CHAPTER 5

Conclusions and Suggested Works

In this thesis, we attempted to fabricate a photovoltaic device based on the rectennae (rectifying antennae) concept. Gold was used as antennae element for its well-known plasmonic properties to absorb light in the optical region. The gold nanoarrays were fabricated by either spinning on the tetrapod supports, or by directly growing gold nanowires through the nanoporous membrane. An alkanethiolate monolayer was self-assembled on the gold antennae arrays to serve as a rectifying barrier.

For the tetrapod arrays, the current peaks occurred at CdSe wavelengths. We concluded that the major photocurrent contribution comes from the semiconducting bandgap excitation of CdSe tetrapods absorbance. The addition of a gold layer by sputtering enhanced the photocurrent ten times, indicating that the gold layer can be considered as an enhancement material for active electron-contributing materials (CdSe tetrapods in this case).

We also grew gold nanowires by template synthesis and identified the tunneling properties of SAM-modified gold film and gold nanoarrays by electrochemical analysis. Through cyclic voltammetry and electrochemical impedance spectroscopy, we were able to calculate the tunneling barrier height. The SAM turned out to be well-formed on the gold film, but had poor coverage and defects on the gold nanoarrays. The calculated tunneling barrier of the SAM-modified film is about 0.5 eV, which is in agreement with the literatures. But the barrier of the SAM-modified gold nanoarrays is on the order of 0.01 eV, which is relatively smaller and can be compared with the thermal molecular vibration energy (kT). This shows that the SAM cannot be assembled on the nanoarrays due to solvent contamination and steric hindrance of the high nanowires packing density

Figure 5.1 shows the modified energy diagram of our optical rectennae system. Instead of the original proposed energy diagram (upper one), the lower one illustrates the actual height of the tunneling barrier (on the order of 0.01 eV) and also takes into account the work function of gold. The gold electrons need to be freed by overcoming the work function (5.1 eV) which corresponds to the plasmon band of 243 nm. The plasmonic resonance between the gold electrons can enhance the electric field, but it is considered rather hard to provide enough energy to free the electron from the gold bulk. Therefore, this band needs to be excited by ultraviolet light that has a higher frequency (and energy) than visible light. Once the electron overcomes the work function, it is easy for the electron to recombine with the gold bulk because the tunneling barrier is comparably small. Such a recombination would reduce the generated photocurrent; this is in agreement with what we observed from the preliminary results.

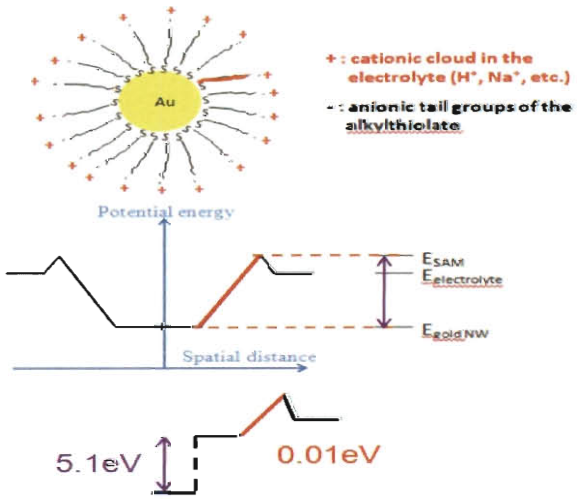

Fig. 5.1 The modified energy diagram considering the work function of gold and also the order of the tunneling barrier height.

Several recommendations can be noted for the future work on this research:

i) Better synthesis and cleaning process for gold nanowires. An apparent disadvantage of growing nanowires via template is that the membrane needs to be dissolved with strong base, which is not easy to remove completely. Using other templates or other

methods (e.g. solution process) to synthesize the gold nanowires could improve the self-assembly of the alkanethiolate monolayers.

ii) Use gold as an enhancement material for other active materials. As an active material, we need to excite the gold out of the bulk to serve as free electrons. Because of its work function, it is rather hard to eject the electrons by exciting the surface plasmon resonance. However, gold has been shown to be a very good material to improve the performance of photovoltaic devices by light trapping and light concentration [117]. Therefore, it is recommended to use gold to enhance the absorption of other materials.

References

(1) Smalley, R. E. *MRS Bulletin* **2005**, *30*, 412-417.

(2) Polman, A.; *Annual Report at Center for Nanophotonics FOM-Institute AMOLF*, Amsterdam, **2008**.

(3) Lewis, N. S. *Science* **2007**, *315*, 798-801.

(4) Green, M. A. *Physica E* **2002**, *14*, 11-17.

(5) Brown, A. S.; Green, M. A.; Corkish, R. P. *Physica E-Low-Dimensional Systems & Nanostructures* **2002**, *14*, PII S1386-9477.

(6) Coakley, K. M.; McGehee, M. D. *Chemistry of Materials* **2004**, *16*, 4533-4542.

(7) Shah, A.; Torres, P.; Tscharner, R.; Wyrsch, N.; Keppner, H. *Science* **1999**, *285*, 692-698.

(8) Brown, W. C. *IEEE Transactions on Microwave Theory and Techniques* **1984**, *32*, 1230-1242.

(9) Berland, B. *ITN Energy System final report*, **2003**.

(10) Link, S.; El-Sayed, M. A. *Journal of Physical Chemistry B* **1999**, *103*, 4212-4217.

(11) Lin, G. H.; Abdu, R.; Bockris, J. O. *Journal of Applied Physics* **1996**, *80*, 565-568.

(12) Reed, M. A.; Zhou, C.; Muller, C. J.; Burgin, T. P.; Tour, J. M. *Science* **1997**, *278*, 252-254.

(13) Tour, J. M. *Accounts of Chemical Research* **2000**, *33*, 791-804.

(14) Rubinstein, I.; Sabatani, E.; Maoz, R.; Sagiv, J. *Organized Monolayers on Gold Electrodes, in Electrochemical Sensors for Biomedical Applications*, C.K.N. Li Ed.; The Electrochemical Society, **1986**.

(15) *World Consumption of Primary Energy by Energy Type and Selected Country Groups: 1980-2004*, Energy Information Administration, **2008**.

(16) Perlin, J. *From Space to Earth: The Story of Solar Electricity*; AATEC Publications: Ann Arbor, MI, **1999**.

(17) Green, M. A. *Progress in Photovoltaics* **2001**, *9*, 123-135.

(18) Wenham, S. R.*Report at ARC Photovoltaics Centre of Excellence*, Sydney, **2007**.

(19) Fox, M.*Optical Properties of Solids*, Oxford Univ. Press: New York, **2003**.

(20) Brown, W. C. *Solar Energy* **1996**, *56*, 3-21.

(21) Bailey, R. L. *Journal of Engineering for Power* **1972**, *94*, 73-77.

(22) Fletcher, J. C.; Bailey, R. L.; United States Patent 3760257, **1973**.

(23) Farber, E. A.; *Report at Airforce* AF C F08635-83-C-0136, Task 85-6, **1988**.

(24) Kraus, J. D. *Antennas*, 2nd Ed.; McGraw-Hill: New York, **1988**.

(25) Marks, A. M.; United States Patent 4574161, **1986**.

(26) Marks, A. M.; United States Patent 4720642, **1988**.

(27) Corkish, R.; Green, M. A.; Puzzer, T. *Solar Energy* **2002**, *73*, 395-401.

(28) Goswami, D. Y.; Vijayaraghavan, S.; Lu, S.; Tamm, G. *Solar Energy* **2004**, *76*, 33-43.

(29) Sarehraz, M.; Buckle, K.; Weller, T.; Stefanakos, E.; Bhansall, S.; Goswami, Y.; Krishnan, S. *IEEE Photovoltaic Specialists Conference*, **2005**.

(30) Lucas, A. A.; Cutler, P. H. *Solid State Communications* **1973**, *13*, 361-365.

(31) Sullivan, T. E.; Cutler, P. H.; Lucas, A. A. *Surface Science* **1976**, *54*, 561-579.

(32) Sullivan, T. E.; Cutler, P. H.; Lucas, A. A. *Surface Science* **1977**, *62*, 455-471.

(33) Oesterschulze, E.; Georgiev, G.; Muller-Wiegand, M.; Vollkopf, A.; Rudow, O. *Journal of Microscopy-Oxford* **2001**, *202*, 39-44.

(34) Schelkunoff, S. A. *Journal of Applied Physics* **1951**, *22*, 1330-1332.

(35) Wu, L. Y.; Ross, B. M.; Lee, L. P. *Nano letters* **2009**, *9*, 1956-1961.

(36) Dresselhaus, M. S. *Nature* **2004**, *432*, 959-960.

(37) Kempa, K.; Rybczynski, J.; Huang, Z. P.; Gregorczyk, K.; Vidan, A.; Kimball, B.; Carlson, J.; Benham, G.; Wang, Y.; Herczynski, A.; Ren, Z. F. *Advanced Materials* **2007**, *19*, 421-426.

(38) Ren, Z.; Kempa, K.; Wang, Y.; United States Patent 0240757, **2007**.

(39) Duque, J. G., *Ph.D. Thesis at Cemical and Biomolecular Engineering*, Rice University, Houston, **2009**.

(40) Grätzel, M. *Nature* **2001**, *414*, 338-344.

(41) Love, J. C.; Estroff, L. A.; Kriebel, J. K.; Nuzzo, R. G.; Whitesides, G. M. *Chemical Reviews* **2005**, *105*, 1103-1169.

(42) Martin, C. R. *Science* **1994**, *266*, 1961-1966.

(43) Asokan, S.; Krueger, K. M.; Colvin, V. L.; Wong, M. S. *Small* **2007**, *3*, 1164-1169.

(44) Novotny, L.; Hecht, B. *Principles of Nano-optics*; Cambridge Univ. Press: New York, **2006**.

(45) Freestone, I.; Meeks, N.; Sax, M.; Higgitt, C. *Gold Bulletin* **2007**, *40/4*.

(46) Mie, G. *Annalen Der Physik* **1908**, *25*, 377-445.

(47) Kretschmann, E. *Zeitschrift für Naturforschung. B* **1968**, *23*, 2135.

(48) Otto, A. *Zeitschrift Für Physik* **1968**, *216*, 398.

(49) Barnes, W. L.; Dereux, A.; Ebbesen, T. W. *Nature* **2003**, *424*, 824-830.

(50) Wu, L. Y.; Ross, B. M.; Lee, L. P. *Nano Letters* **2009**, *9*, 1956-1961.

(51) Hao, F.; Nehl, C. L.; Hafner, J. H.; Nordlander, P. *Nano Letters* **2007**, *7*, 729-732.

(52) Homola, J.; Yee, S. S.; Gauglitz, G. *Sensors and Actuators B-Chemical* **1999**, *54*, 3-15.

(53) Karlsson, R.; Michaelsson, A.; Mattsson, L. *Journal of Immunological Methods* **1991**, *145*, 229-240.

(54) Jonsson, U.; Fagerstam, L.; Ivarsson, B.; Johnsson, B.; Karlsson, R.; Lundh, K.; Lofas, S.; Persson, B.; Roos, H.; Ronnberg, I.; Sjolander, S.; Stenberg, E.;

Stahlberg, R.; Urbaniczky, C.; Ostlin, H.; Malmqvist, M. *Biotechniques* **1991**, *11*, 620.

(55) Pyayt, A. L.; Wiley, B.; Xia, Y. N.; Chen, A.; Dalton, L. *Nature Nanotechnology* **2008**, *3*, 660-665.

(56) Stockman, M. I. *Physical Review Letters* **2004**, *93*, 137404.

(57) Maier, S. A.; Kik, P. G.; Atwater, H. A. *Applied Physics Letters* **2002**, *81*, 1714-1716.

(58) Knight, M. W.; Grady, N. K.; Bardhan, R.; Hao, F.; Nordlander, P.; Halas, N. J. *Nano Letters* **2007**, *7*, 2346-2350.

(59) Nie, S. M.; Emery, S. R. *Science* **1997**, *275*, 1102-1106.

(60) Otto, A.; Mrozek, I.; Grabhorn, H.; Akemann, W. *Journal of Physics-Condensed Matter* **1992**, *4*, 1143-1212

(61) Radecka, M. *Materials Science-Poland* **2006**, *24*, 285-290.

(62) Thio, T.; United States Patent 6441298, **2002**.

(63) Eustis, S.; El-Sayed, M. A. *Chemical Society Reviews* **2006**, *35*, 209-217.

(64) Prodan, E.; Nordlander, P.; Halas, N. J. *Nano Letters* **2003**, *3*, 1411-1415.

(65) Maier, S. A.; Atwater, H. A. *Journal of Applied Physics* **2005**, *98,* 011101.

(66) Liz-Marz´an, L. M. *Langmuir*, **2006**, *22*, 23-32.

(67) Link, S.; El-Sayed, M. A. *J. Phys. Chem. B* **2005**, *109*, 10531.

(68) Yu, Y. Y.; Chang, S. S.; Lee, C. L.; Wang, C. R. C. *Journal of Physical Chemistry B* **1997**, *101*, 6661-6664.

(69) Wang, J.; Zeng, B. Z.; Fang, C.; Zhou, X. Y. *Journal of Electroanalytical Chemistry* **2000**, *484*, 88-92.

(70) Yang, L.; Wei, W. Z.; Xia, J. J.; Tao, H.; Yang, P. H. *Analytical Sciences* **2005**, *21*, 679-684.

(71) Schwartz, D. K. *Annu. Rev. Phys. Chem.* **2001**, *52,* 107.

(72) Nuzzo, R. G.; Allara, D. L. *Journal of the American Chemical Society* **1983**, *105*.

(73) Xu, J.; Li, H. L.; Zhang, Y. *Journal of Physical Chemistry* **1993**, *97*, 11497-11500.

(74) Finklea, H. In *Electroanalytical Chemistry*; Bard, A., Rubinstein, I., Marcel Dekker, Inc.: New York, **1996.**

(75) Bard, A., L. Faulkner *Electrochemical methods: fundamentals and applications*, 2nd Ed; John Wiley & Sons, Inc.: Hoboken, NJ, **2001**.

(76) Diao, P.; Jiang, D. L.; Cui, X. L.; Gu, D. P.; Tong, R. T.; Zhong, B. *Journal of Electroanalytical Chemistry* **1999**, *464*, 61-67.

(77) Gamry Instrument, *In Electrochemical Impedance Spectroscopy Theory: A Primer*; **2010**.

(78) Chirea, M.; Cruz, A.; Pereira, C. M.; Silva, A. F. *Journal of Physical Chemistry C* **2009**, *113*, 13077-13087.

(79) Alivisatos, A. P. *Science* **1996**, *271*, 933-937.

(80) Mokari, T.; Rothenberg, E.; Popov, I.; Costi, R.; Banin, U. *Science* **2004**, *304*, 1787-1790.

(81) Manna, L.; Scher, E. C.; Alivisatos, A. P. *Journal of the American Chemical Society* **2000**, *122*, 12700-12706.

(82) Milliron, D. J.; Hughes, S. M.; Cui, Y.; Manna, L.; Li, J. B.; Wang, L. W.; Alivisatos, A. P. *Nature* **2004**, *430*, 190-195.

(83) Hulteen, J. C.; Martin, C. R. *Journal of Materials Chemistry* **1997**, *7*, 1075-1087.

(84) Wirtz, M.; Martin, C. R. *Advanced Materials* **2003**, *15*, 455-458.

(85) Fleisher, R. L.; Price, P. B.; Walker, R. M. *Nuclear Tracks in Solids*; University of California Press, Berkeley: CA, **1975**.

(86) Despic, A.; Parkhutik, V. P. *Modern Aspects of Electrochemistry*; White and B. E. Conway, Plenum Press: New York, **1989**.

(87) Kline, T. R.; Tian, M. L.; Wang, J. G.; Sen, A.; Chan, M. W. H.; Mallouk, T. E. *Inorganic Chemistry* **2006**, *45*, 7555-7565.

(88) Li, Q. C.; Kumar, V.; Li, Y.; Zhang, H. T.; Marks, T. J.; Chang, R. P. H. *Chemistry of Materials* **2005**, *17*, 1001-1006.

(89) Sander, M. S.; Cote, M. J.; Gu, W.; Kile, B. M.; Tripp, C. P. *Advanced Materials* **2004**, *16*, 2052-2057.

(90) Kohli, P.; Wharton, J. E.; Braide, O.; Martin, C. R. *Journal of Nanoscience and Nanotechnology* **2004**, *4*, 605-610.

(91) Zhang, X.; Wang, H.; Bourgeois, L.; Pan, R.; Zhao, D.; Webley, P. A. *Journal of Materials Chemistry* **2008**, *18*, 463-467.

(92) Schuchert, I. U.; Toimil-Molares, M. E.; Dobrev, D.; Vetter, J.; Neumann, R.; Martin, M. *Journal of the Electrochemical Society* **2003**, *150*, C189-C194.

(93) Motoyama, M.; Fukunaka, Y.; Sakka, T.; Ogata, Y. H.; Kikuchi, S. *Journal of Electroanalytical Chemistry* **2005**, *584*, 84-91.

(94) Tian, M. L.; Wang, J. U.; Kurtz, J.; Mallouk, T. E.; Chan, M. H. W. *Nano Letters* **2003**, *3*, 919-923.

(95) Wang, J. G.; Tian, M. L.; Mallouk, T. E.; Chan, M. H. W. *Nano Letters* **2004**, *4*, 1313-1318.

(96) Liu, J.; Duan, J. L.; Toimil-Molares, E.; Karim, S.; Cornelius, T. W.; Dobrev, D.; Yao, H. J.; Sun, Y. M.; Hou, M. D.; Mo, D.; Wang, Z. G.; Neumann, R. *Nanotechnology* **2006**, *17*, 1922-1926.

(97) Bauer, L. A.; Birenbaum, N. S.; Meyer, G. J. *Journal of Materials Chemistry* **2004**, *14*, 517-526.

(98) Liu, H. T.; Alivisatos, A. P. *Nano Letters* **2004**, *4*, 2397-2401.

(99) Li, J.; Kaifer, A. E. *Langmuir* **1993**, *9*, 591-596.

(100) Suga, K.; Bradley, M.; Rusling, J. F. *Langmuir* **1993**, *9*, 3063-3066.

(101) Bashar, H. A., Ph. D. *Thesis at Electronic and Electrical Engineering*, University of London, London, **1998**.

(102) Cerruti, M.; Rhodes, C.; Losego, M.; Efremenko, A.; Maria, J. P.; Fischer, D.; Franzen, S.; Genzer, J. *Journal of Physics D-Applied Physics* **2007**, *40*, 4212-4221.

(103) Yan, C.; Zharnikov, M.; Golzhauser, A.; Grunze, M. *Langmuir* **2000**, *16*, 6208-6215.

(104) Suzuki, H. *Japanese Journal of Applied Physics* **1966**, *5*, 879-885.

(105) Bandyopadhyay, K.; Vijayamohanan, K.; Manna, A.; Kulkarni, B. D. *Journal of Colloid and Interface Science* **1998**, *206*, 224-230.

(106) van der Zande, B. M. I.; Bohmer, M. R.; Fokkink, L. G. J.; Schonenberger, C. *Langmuir* **2000**, *16*, 451-458.

(107) Liu, L.; Lee, W.; Huang, Z.; Scholz, R.; Gosele, U. *Nanotechnology* **2008**, *19*, 335604.

(108) Evans, P.; Hendren, W. R.; Atkinson, R.; Wurtz, G. A.; Dickson, W.; Zayats, A. V.; Pollard, R. J. *Nanotechnology* **2006**, *17*, 5746-5753.

(109) Widrig, C. A.; Chung, C.; Porter, M. D. *Journal of Electroanalytical Chemistry* **1991**, *310*, 335-359.

(110) Rampi, M. A.; Schueller, O. J. A.; Whitesides, G. M. *Applied Physics Letters* **1998**, *72*, 1781-1783.

(111) Ding, S. J.; Chang, B. W.; Wu, C. C.; Lai, M. F.; Chang, H. C. *Analytica Chimica Acta* **2005**, *554*, 43-51.

(112) Bain, C. D.; Troughton, E. B.; Tao, Y. T.; Evall, J.; Whitesides, G. M.; Nuzzo, R. G. *Journal of the American Chemical Society* **1989**, *111*, 321-335.

(113) Dijksma, M.; Boukamp, B. A.; Kamp, B.; van Bennekom, W. P. *Langmuir* **2002**, *18*, 3105-3112.

(114) Cecchet, F.; Fioravanti, G.; Marcaccio, M.; Margotti, M.; Mattiello, L.; Paolucci, F.; Rapino, S.; Rudolf, P. *Journal of Physical Chemistry B* **2005**, *109*, 18427-18432.

(115) Porter, M. D.; Bright, T. B.; Allara, D. L.; Chidsey, C. E. D. *Journal of the American Chemical Society* **1987**, *109*, 3559-3568.

(116) Miller, C., Cuendet, P., Gratzel M. *J. Phys. Chem.* **1991**, *95*, 877-886.

(117) Atwater, H. A.; Polman, A. *Nature Materials* **2010**, *9*, 205-213.